Aerosol dynamic processes in the Hunga plume in January 2022: Does water vapor accelerate aerosol aging?

Julia Bruckert[1], Simran Chopra[1], Richard Siddans[2,3], Charlotte Wedler[1], and Gholam Ali Hoshyaripour[1]

[1] Institute of Meteorology and Climate Research Tropospheric Research (IMKTRO), Karlsruhe Institute of Technology (KIT), Karlsruhe, Germany
[2]Remote Sensing Group, STFC Rutherford Appleton Laboratory, Chilton, UK
[3]National Centre for Earth Observation, STFC Rutherford Appleton Laboratory, Chilton, UK

Correspondence: Julia Bruckert (julia.bruckert@kit.edu)

Abstract. The 2022 Hunga eruption injected an unprecedented ~~amount of~~ 150 Tg of water vapor into the stratosphere, accelerating SO_2 oxidation and sulfate aerosol formation. Despite releasing less ash than previous eruptions of similar magnitude, the role of ash in the early plume and its rapid removal remains unclear. We performed experiments with the ICOsahedral Nonhydrostatic model with Aerosols and Reactive Tracers (ICON-ART) to better understand the role of water vapor, SO_2 and ash ~~emission~~emissions, aerosol-radiation interaction, and aerosol dynamical processes (nucleation, condensation, coagulation) in the Hunga plume in the first week after the eruption. Furthermore, we compared our results ~~to~~ with satellite observations to validate SO_2 oxidation and aerosol dynamical processes. Our results show that about 1.2 Tg of SO_2 emission ~~as well as~~ along with water vapor emission is necessary to explain both the SO_2 column loadings and sulfate aerosol optical depth during the first week after the eruption. Although the model reproduces ~~well~~ the development of SO_2 and sulfate aerosols well, the aerosol dynamics alone cannot explain the ash removal after the eruption, as was seen in satellite images. However, some of the ash might not be detected ~~because of~~ due to the exceptionally strong coating of the ash particles. Both ~~,~~ the strong coating and a doubling of the sulfate effective radii within one week, occur only when ~~the~~ water vapor emission is ~~considered~~ included in the chemistry. Furthermore, aerosol-radiation interaction warms the plume and reduces or, depending on the ~~experiments~~experiment, even reverses the descent of the water vapor plume ~~due to~~ that would otherwise occur due radiative cooling.

1 Introduction

Volcanic eruptions emit tephra and gases such as water vapor and sulfur dioxide (SO_2) into the atmosphere. Chemical reactions oxidize SO_2 to sulfuric acid (H_2SO_4) and subsequent sulfate production can form secondary aerosol particles. Both ~~directly emitted primary aerosols (such as~~ primary (e.g., volcanic ash) ~~as well as~~ and secondary aerosol components ~~can~~ (e.g., sulfate) interact with radiation (Niemeier et al., 2009; Muser et al., 2020) and clouds (Malavelle et al., 2017; Haghighatnasab et al., 2022) and ~~, thereby,~~ therefore affect weather and climate (Robock, 2000; Timmreck, 2012).

Aerosol-radiation interaction (ARI) leads to a warming and lofting of volcanic plumes ~~(e.g., Muser et al., 2020; Stenchikov et al., 2021)~~ (e.g., Muser et al., 2020; Stenchikov et al., 2021; Ukhov et al., 2023), which can increase the lifetime of volcanic aerosols in the plume. The lifetime of aerosols depends, among ~~others~~other factors, on the ~~size of the particles~~ particle size distribution

which can be ~~modified~~ altered by aerosol dynamical processes ~~(~~such as nucleation, condensation, coagulation, ~~sedimentation)~~and sedimentation. Muser et al. (2020) showed that ~~volcanic ash aging, i.e.,~~ the aging of volcanic ash, characterized by a coating of soluble components (mainly sulfate and water in volcanic plumes) on insoluble aerosols (here ash), ~~leads to a faster removal of the~~ accelerates the removal of particles from the atmosphere. Aerosol aging is faster in the troposphere than in the stratosphere, most likely due to the higher humidity (Bruckert et al., 2023). The lifetime of chemical compounds such as SO_2 depends on the oxidation capacity of the surrounding air. Although Sioris et al. (2016) found that moderate-size eruptions (volcanic explosivity index ~~(VEI)~~ 4 – 5) do not provide an effective mechanism for large-scale hydration of the stratosphere, it has been shown that water vapor can locally change the atmospheric chemistry by the formation of OH (Bekki, 1995; LeGrande et al., 2016) or increase the oxidation rate of SO_2 to sulfate in Pinatubo-size eruptions (Abdelkader et al., 2023). Furthermore, Zhu et al. (2020) showed that the presence of ash can increase the removal of SO_2 from the atmosphere by adsorption on the ash surfaces and subsequent sedimentation.

The eruption of the Hunga submarine volcano (20.6°S, 175.4°W) on 15 January 2022 was outstanding in the satellite era. Never before has an eruption been instrumentally observed with such high water vapor emissions reaching up into the ~~strato-~~stratosphere and mesosphere. Umbrella plume top heights of about 31 km (Gupta et al., 2022) to 40 km with overshooting tops of about 55-57 km (Carr et al., 2022; Proud et al., 2022) were observed by satellite measurements. Observations in the following days reveal the main transport altitude to be above 25 km (Asher et al., 2023; Taha et al., 2022; Khaykin et al., 2022).

The observed water vapor emission ranges between more than 50 Tg (Vömel et al., 2022) and around 139 - 150 Tg (Millán et al., 2022; Xu et al., 2022; Khaykin et al., 2022), which is approximately 10% of the stratospheric water vapor burden. Carn et al. (2022) estimated an SO_2 emission of about 0.4-0.5 Tg. However, Sellitto et al. (2022) investigated satellite observations of the first days after the eruption and reported a maximum in the SO_2 burden of about 1.0 Tg on 18 January 2022, three days after the eruption. They argued that the instruments might have been saturated in the first days of the eruption and/or that ash and ice covered parts of the SO_2 plume.

Both modeling and observation studies show an exceptionally fast oxidation of SO_2 probably due to the large co-emission of water vapor (Zhu et al., 2022; Asher et al., 2023), which leads to a quick formation of sulfate aerosols (Sellitto et al., 2022; Zhu et al., 2022). The derived e-folding times range between 6 and 15 days (6 days in Carn et al. (2022), 12 days in Zhu et al. (2022); Asher et al. (2023), 15 days in Sellitto et al. (2022)). Asher et al. (2023) estimated from balloon-borne instrumentations that the sulfate formation was complete within the first three weeks after the eruption, i.e., the conversion of SO_2 ~~was~~ occurred about three times faster than expected under ~~climatological~~ typical stratospheric conditions.

Aerosol dynamical processes modify the radius of aerosol particles. For instance, nucleation and sedimentation reduce the median radius of an aerosol distribution, whereas coagulation and condensation increase the median radius. Boichu et al. (2023) investigated aerosol data from 20 AERONET (AErosol RObotic NETwork) stations. Their evaluation show a doubling of the radius within the first week after the eruption (peak radius of 0.22-0.26 μm one day after the eruption to 0.4-0.5 μm about one week after the eruption). Asher et al. (2023) measured an effective diameter of up to 1.5 μm (mode median effective diameter at 560 nm) during their measurement campaign at Réunion island 7-10 days after the eruption.

Satellite observations revealed the presence of ash and ice in the early eruption plume, but these components seem to be quickly removed from the dispersing plume, as for instance revealed from ~~CALIPSO (Cloud–Aerosol Lidar and Infrared Pathfinder Satellite Observation) and HIMAWARI-8~~ CALIOP (Cloud-Aerosol Lidar with Orthogonal Polarization) and Himawari-8 data (e.g., Sellitto et al., 2022; Legras et al., 2022; Khaykin et al., 2022). However, Boichu et al. (2023) found an indication of coated ash particles one week after the eruption (poorly absorbing coarse particles with an effective radius of 4.6 μm), which would appear as spherical particles in satellite products such as CALIOP. Kloss et al. (2022) also observed absorbing and semi-transparent particles with radii <0.5 μm in balloon flights at La Réunion on 23 and 26 January 2022. They argue that these particles could be either small sulfate-coated ash particles or a thin ash layer below a sulfate aerosol layer. Furthermore, Baron et al. (2023) argued that presence of fine ash, indicated by higher absorption capabilities, could not be ruled out from their lidar measurements.

Accurate modeling of the dispersion and processes in the early stage of volcanic plumes strongly depends on the knowledge of the eruption source parameters~~(ESPs), i.e.,~~ i.e., the plume height, the mass eruption rate (MER) of the main plume constituents (ash, SO_2, water vapor), the emission profile (e.g., Scollo et al., 2008; Harvey et al., 2018), and the timing of the eruption phases (Bruckert et al., 2022). Both timing and plume height can be derived from satellite measurements. The MER is often derived from plume heights using one-dimensional (1-D) plume models (e.g., Mastin, 2007; Folch et al., 2016), which require estimates of volcanic conditions such as exit temperature, exit velocity, and exit volatile fraction. The total MER and volcanic source conditions for the Hunga eruption were estimated with the 1D volcanic plume rise model Plumeria (Mastin, 2007) in Mastin et al. (2024). They found that the plume had to consist of 90% steam (water vapor at 100°C) from the ocean in order to be consistent with the tephra fallout measurements around the volcano.

The Hunga eruption emitted material in multiple eruption phases, which are indicated by several types of instruments and methods (e.g., satellite images (Gupta et al., 2022), ionospheric observations of the total electron content (Astafyeva et al., 2022), damage of seafloor cables (Clare et al., 2023), back-propagation of atmospheric waves (Horváth et al., 2024; Matoza et al., 2022; Podglajen et al., 2022; Wright et al., 2022), tsunami simulations (Purkis et al., 2023)). Although all these instruments and methods come up with slightly different timings due to ~~the~~ differences in measurement types and the fact that explosions and emissions ~~are not necessarily the same~~do not necessarily coincide, the main ~~agreement relevant for~~ point of agreement relevant to this paper is ~~:~~ that two major emissions into the atmosphere occurred on 15 January 2022 between 4:00 and 5:00 UTC (Gupta et al., 2022) with a complex eruption sequence of multiple pulses (Astafyeva et al., 2022; Clare et al., 2023; Matoza et al., 2022; Horváth et al., 2024; Podglajen et al., 2022; Purkis et al., 2023; Wright et al., 2022), and a final explosion occurred between 8:00 and 9:00 UTC (Gupta et al., 2022; Matoza et al., 2022; Horváth et al., 2024; Podglajen et al., 2022).

In this paper, we investigate aerosol dynamical processes in the early Hunga plume with the aim to answer the following research questions: ~~Can model simulations help to constrain the~~ Which SO_2 mass injection into the stratosphere during the Hunga eruption is needed to reproduce the observed evolution of both SO_2 and sulfate? Can aerosol dynamics including ash and sulfate explain the quick loss of ash on the first day of the eruption? What is the role of the emission of water vapor, SO_2, and ash, ~~and of ARI~~as well as ARI, in the evolution of the particle effective radius~~.~~? This paper is structured as follows:

Section 2 ~~introduces~~ presents the model and its setup used for this study, the experiments, and the observations for the model validation. The results are split into three sections: 1. we analyze the contribution of the emission of SO_2, water vapor, and ash, and ARI to the development of the early Hunga plume (~~section~~Sect. 3); 2. we validate our results with observations with respect to transport, SO_2 oxidation and sulfate formation (~~section~~Sect. 4); 3. we investigate the contribution of different in-plume processes (ARI, coagulation, emission of water vapor and ash) to the development of the particle effective radius. Finally, we conclude our results in ~~section~~Sect. 6 and discuss limitations of the model setup.

In this paper, we consistently use the term 'volcanic water vapor' to describe the water vapor released into the stratosphere as a result of the Hunga eruption. While most of this water vapor comes from evaporating ocean water (Mastin et al., 2024) (external water), the plume can also contain volcanological water vapor and entrained water vapor during its ascent.

2 Data and Methods

In this section, the modeling system as well as the observational data used for validation are described.

2.1 ICON-ART modeling system

The ICOsahedral Nonhydrostatic (ICON) model is a weather and climate model, which allows seamless predictions from local to global scale (Zängl et al., 2015; Heinze et al., 2017; Giorgetta et al., 2018). ICON solves the three-dimensional nonhydrostatic and compressible Navier-Stokes equations on a triangular icosahedral grid. ICON's submodule ART (Aerosols and Reactive Trace gases) considers emissions, atmospheric processes, and removal of aerosols and chemical tracers (Rieger et al., 2015). ICON-ART can be configured for large-eddy, numerical weather prediction (NWP), and climate simulations. In this study we use an NWP configuration explained below. A detailed description of the ART features used for this study is given in chapter 2.1.2.

2.1.1 Microphysics scheme in ICON

Water vapor undergoes temperature-dependent phase changes in the atmosphere. Here, we used ICON's one-moment microphysics scheme considering five water tracers, namely water vapor q_v, cloud water q_c, rain water q_r, cloud ice q_i, and snow q_s. The phase transition between q_v and q_c is calculated ~~by~~ via saturation adjustment, i.e., a parametrization which ensures that vapor and liquid ~~phase~~ phases are in equilibrium (Prill et al., 2023). ~~The transfer rates between the other water tracers are calculated with parametrizations which assume~~ Other transitions (e.g., between cloud water and rain or snow) are governed by non-equilibrium ~~processes~~ parametrizations (Doms et al., 2018).

Large emissions of water vapor into ICON-ART by~~e.g.,~~ , for example, a volcanic eruption such as the Hunga eruption, without using any temperature adjustments (as assumed by Niemeier et al. (2023)), ~~leads to a quick~~ lead to a rapid formation of liquid and solid water, which was also found in other models (Stenchikov et al., 2021). ~~Nevertheless~~Despite this, the total water mass is conserved in ICON-ART (not shown).

2.1.2 Chemistry and aerosol processes

We represent the gas-phase oxidation of SO_2 to H_2SO_4 by means of ART's simplified OH-chemistry mechanism ~~, which has been implemented by Weimer et al. (2017)~~(Weimer et al., 2017). In this mechanism, the oxidation of chemical species such as CH_4 and SO_2 depends on the abundance of OH, which is parameterized as a function of water vapor and ozone ~~number~~ concentrations. The ozone concentration is derived from the stratospheric LINOZ (linearized ozone) scheme ~~by McLinden et al. (2000)~~(McLinden et al., 2000), where the ozone concentration tendency is linearized with respect to the local ozone mixing ratio, temperature and overhead ozone column density. The simplified OH-chemistry together with the LINOZ scheme has been applied and validated against observations for the volcanic plumes of the 2019 Raikoke eruption (Muser et al., 2020; Bruckert et al., 2023) and the 2021 La Soufrière eruption (Bruckert et al., 2023).

~~The~~ ART's aerosol dynamics module ~~(AERODYN) in ART~~ considers the formation of sulfate and the aging of particles. The details are described in Muser et al. (2020). We assumed seven log-normal modes, including Aitken mode (as soluble), accumulation modes (as soluble, insoluble, and mixed), coarse modes (as insoluble and mixed) and a giant (as insoluble) mode.

We emitted volcanic ash into the insoluble modes. By nucleation, H_2SO_4 can form sulfate in the soluble Aitken mode. Condensation of H_2SO_4 on existing particles and coagulation of particles (inter- and intramodal) lead to growth of particles and changes in the mixing state. Two mechanisms can shift particles from one mode to another. The first mechanism shifts particles from the soluble Aitken to the soluble accumulation mode if a diameter threshold of 0.03 μm is exceeded. If a mass fraction of soluble coating on insoluble particles exceeds 5%, the second mechanism shifts particles from the insoluble mode to the corresponding mixed mode.

The process of coagulation in ICON-ART is based on the parametrization by Riemer (2002) and only includes coagulation due to Brownian motion. The interaction of ash due to electrostatic forces and the dependence on water (wet aggregation), which is important in very dense plumes (i.e., in the first minutes of volcanic eruptions), are not considered.

In ART, water uptake by aerosol particles is realized by the ISORROPIA II model, which calculates gas-aerosol partitioning according to thermodynamic equilibrium (Fountoukis and Nenes, 2007). ~~The interaction of aerosolsand radiation is described in Muser et al. (2020)~~

The ecRad model by Hogan and Bozzo (2018) calculates the radiative fluxes in ICON. It requires the mass extinction coefficient, the single scattering albedo, and the asymmetry parameter to account for the radiative effects of aerosols. For all modes, these properties were derived offline and individually based on Mie calculations and stored in look-up tables for online calculations of ARI (Muser et al., 2020).

2.1.3 Volcanic emissions

Volcanic emissions in ICON-ART are calculated online with the 1-D volcanic plume rise model FPlume by Folch et al. (2016). FPlume calculates a total MER based on a given plume height. As input parameters for the plume dynamics, FPlume requires exit temperature, exit velocity, and exit volatile fraction as well as atmospheric profiles above the vent for pressure, temperature, specific humidity and density (Folch et al., 2016). ~~Details on the~~ The parametrization by Gouhier et al. (2019) calculates the

fraction of very fine ash (particles $<30\ \mu m$), which is relevant for atmospheric transport, from the given height and the calculated MER. The MER of SO_2 is prescribed based on observations and emitted in the same emission phases as for ash. The vertical distribution of all emitted masses (here ash, H_2O and SO_2) is calculated according to the Suzuki profiles (Suzuki, 1983) . Further details on the coupling of ICON-ART and FPlume are given in Bruckert et al. (2022). Figure A1 shows the emission profiles as well as the vertical distribution of ash, SO_2, and water vapor after the beginning of the first emission phase.

The coupling of ICON-ART with FPlume has been validated against observations for the 2019 Raikoke eruption (Bruckert et al., 2022) and the 2021 La Soufrière eruption (Bruckert et al., 2023). Different from previous ~~works~~work with ICON-ART coupled to FPlume, which considered only ash and SO_2 emissions, we additionally emitted water vapor in this study. We assumed the amount of entrained water to be small compared to the water vapor injected into the atmosphere due to the Hunga eruption and, therefore, we derived the MER of water vapor from the product of the total MER (from FPlume) and the exit volatile fraction (FPlume does not distinguish between water vapor and volatiles). This derived water vapor MER is added to ICON's water vapor mixing ratio. The phase partitioning between vapor, liquid and solid hydrometeors is calculated in ICON's microphysics scheme (Sect. 2.1.1). In order to avoid FPlume from reading meteorological profiles which are strongly affected by the emission from the previous time step, we provided averaged profiles from an external file instead of the profiles from the ICON model at every time step.

The input parameters used for FPlume for the eruption phases are summarized in Table 1. We chose the same values for both eruption phases, because the uncertainty range of the measurement is large and detailed information on plume dynamics during both phases is lacking. Furthermore, we used a plume top height of 33.7 km, which is in the uncertainty range of observations of the umbrella plume (~~e.g.,~~ neglecting the overshooting top) (e.g., Gupta et al., 2022) and also ensures that approximately 150 Tg water vapor remains in the stratosphere after the emission (phase-transition depends on temperatures and therefore, the injection height). In our simulations, about 500 Tg ~~solid and~~ of solid hydrometeors (ice and snow) and less than 50 Tg ~~liquid hydrometeors enter~~ of liquid hydrometeors (cloud and rain water) are released into the stratosphere, which subsequently fall out in the first 1-2 days.

2.2 Model setup and experiments

We performed seven experiments to investigate the role of water vapor, ash, and aerosol dynamics in the first week after the Hunga eruption. The assumptions for the experiments are summarized in Table 2. ~~For all experiments, we performed global simulations with~~ All simulations were performed globally using a horizontal grid spacing of ~~about~~ approximately 40 km (~~R2B06~~R02B06) and 90 vertical levels ~~,~~ resolving the atmosphere up to a height of 75 km. ~~The simulations are initialized with analysis fields~~ For each experiment, we simulated seven days initialized on 15 January 2022 at 00:00 UTC with analysis data provided by the German Weather Service (~~Deutscher Wetterdienst (DWD)).~~ DWD). The analysis data contained variables describing the atmospheric state, variables needed by the land component, and sea surface temperatures. Due to the short time span of the simulation, sea surface temperatures are temporally fixed throughout the simulation.

The first estimate of the SO_2 mass in Carn et al. (2022) was on the order of 0.4-0.5 Tg. We therefore used 0.4 Tg in the experiment $1/3xSO_2$, similar to the modeling study by Zhu et al. (2022). However, Sellitto et al. (2022) argued that the

Category	Parameter	~~Phase 1~~ Phase 1	~~Phase 2~~ Phase 2
Assumptions	~~plume~~ Plume height	33.7 km	33.7 km
	~~timing~~ Timing	~~4.00~~ 4:00 - ~~5.00~~5:00 UTC	~~8.00~~ 8:00 - ~~9.00~~9:00 UTC
	~~exit~~ Exit temperature	100°C	100°C
	~~exit~~ Exit velocity	225 m/s	225 m/s
	~~exit~~ Exit volatile fraction	90%	90%
	MER SO_2 (Reference experiment)	1.67×10^5 kg/s	1.67×10^5 kg/s
Calculated during the simulation	~~total~~ Total MER	1.20×10^8 kg/s	1.20×10^8 kg/s
	MER of very fine ash	1.58×10^5 kg/s	1.58×10^5 kg/s
	MER of water vapor	1.08×10^8 kg/s	1.08×10^8 kg/s

Table 1. Summary of the assumptions (top) and FPlume-derived MERs (bottom). The plume heights for the umbrella top heights are from Gupta et al. (2022). The MER of SO_2 was derived from the total mass of 1.2 Tg SO_2 after the eruption (Sellitto et al. (2022, 2024) estimated an emission of more than 1.0 Tg). The values for exit temperature, exit velocity and exit volatile fraction were taken from ~~Plumeria experiments by~~ Mastin et al. (2024).

~~Experiment name~~ Experiment name	~~Ash emission~~ Ash emission	~~Aerosol-radiation interaction~~ ARI	~~SO_2 emission~~ SO_2 emission	~~H_2O emi~~
noVolc	no emission	–	no emission	
Reference	from FPlume	yes	1.2 Tg	coup
1/3xSO_2	from FPlume	yes	0.4 Tg	coup
noH_2Ochem	from FPlume	yes	1.2 Tg	no cou
noAsh	no emission	yes	1.2 Tg	coup
noARI	from FPlume	no	1.2 Tg	coup
noCoag	from FPlume	yes	1.2 Tg	coup

Table 2. Experiments performed for this study.

190 measurements might have underestimated the SO_2 concentration on the first day. Based on their analysis, Sellitto et al. (2022) proposed a value of at least 1 Tg SO_2 entering the stratosphere during the eruption. Thus, for the experiments Reference, noH_2Ochem, noARI, noAsh, and noCoag we tripled the SO_2 emission compared to the experiment 1/3xSO_2.

The mass of very fine ash was evenly distributed into the three insoluble modes (accumulation, coarse, and giant mode) with median diameters of 0.8, 2.98 and 11.35 μm, respectively, and a standard deviation of 1.4 (Muser et al., 2020). The emission
195 of the number density is derived from the emitted mass and the definition of the lognormal distributions.

The observed umbrella radius was expanding to about 80 km (Carr et al., 2022) at 04:30 UTC. Therefore, we distributed the emissions horizontally into ten cells covering an area of approximately 16000 km^3, which is equivalent to the area covered by a circle ~~of~~ with a radius of 71 km.

2.3 Observations and Methods

In this study, we used observations from the CALIOP instrument for the validation of the aerosol and hydrometeor transport, Ozone Mapping and Profiler Suite (OMPS) SO_2 column loadings for the validation of SO_2 oxidation and transport, and Infrared Microwave Sounding / Infrared Atmospheric Sounding Interferometer (IMS/IASI) sulfate ~~Aerosol Optical Depth~~ aerosol optical depth (SAOD) for the validation of the sulfate formation and transport.

2.3.1 CALIOP

The CALIOP instrument aboard the CALIPSO (Cloud-Aerosol Lidar and Infrared Pathfinder Satellite Observations) satellite provides high-resolution vertical profiles of aerosols and clouds since May 2016. The measurements are based on the backscattered signal at 532 nm and 1064 nm. Two channels receive orthogonally polarized components of the 532 nm backscattered signal, whereas the 1064 nm backscatter intensity is only received at one channel (Winker et al., 2009). We used total attenuated backscatter (ATB) signals and depolarization ratios at 532 nm from the CALIOP instrument to validate the simulated aerosol plume transport (L1 data version 4.11 downloaded from https://asdc.larc.nasa.gov/data/CALIPSO/LID_L1-Standard-V4-11/2022/01/).

The ICON-ART ATB signals were calculated offline from simulated aerosol mass mixing ratios with the forward operator described in Hoshyaripour et al. (2019) and applied to volcanic plumes in Bruckert et al. (2023). In total, nine CALIPSO overpasses traversed the Hunga plume within the first week after the eruption.

2.3.2 OMPS

We validated the modeled transport and SO_2 oxidation with SO_2 column loadings from the OMPS nadir mapper (NM, data product OMPS_NPP_NMSO2_PCA_L2, downloaded from https://search.earthdata.nasa.gov/search). OMPS is ~~a~~ an ultraviolet (UV) satellite sensor on ~~NASA/NOAA's~~ the Suomi-National Polar-orbiting Partnership (Suomi-NPP) satellite by the National Aeronautics and Space Administration (NASA) and the National Oceanic and Atmospheric Administration (NOAA) operating since 2011 (Carn et al., 2015). It measures the backscattered UV radiance spectra between 300 to 380 nm wavelength with a spectral resolution of 1 nm. The instruments provides a daily global coverage, which is achieved with a 2800 km cross-track swath with a nadir pixel size of 50 km x 50 km (Carn et al., 2015).

2.3.3 IMS/IASI

~~Metop~~ IASI is a nadir viewing infra-red Fourier transform spectrometer on ~~Metop~~ the MetOp A, B and C satellites which provides spectra at 0.5 cm^{-1} apodised resolution, sampled every 0.25 cm^{-1}, from 625 to 2760 cm^{-1} (Blumstein et al., 2004). Spectra are measured with four detectors, each with a circular field of view ~~(FOV)~~ on the ground (at nadir) of approximately 12 km diameter, arranged in a 2 x 2 grid within a 50 x 50 km^2 field-of-regard (FOR). IASI scans to provide 30 FOR (i.e., 120 individual spectra) evenly distributed across a 2200 km wide swath. ~~Metop~~ MetOp is in sun-synchronous polar orbit with a

local time of descending node crossing of 9:30. It therefore provides almost complete global coverage twice per day at 9:30 and 21:30 local time.

The Rutherford Appleton Laboratory (RAL) IMS scheme employs the optimal estimation method (Rodgers, 2000) to jointly retrieve atmospheric and surface parameters from IASI (in combination with the microwave sounders also on ~~Metop~~MetOp) (Siddans, 2023). The scheme uses the RTTOV 12 (Radiative Transfer for the TIROS Operational Vertical Sounder (TOVS)) radiative transfer model (Saunders et al., 2017) to simulate measured spectra including the effects of aerosol. IMS retrieves the ~~optical depth of sulfate aerosol~~ SAOD at 1170 cm^{-1} (8.5 μm) (i.e., at the peak of the sulfate aerosol mid-infrared extinction cross section), making the following assumptions to define the profile shape and optical properties: (1) The aerosol extinction coefficient profile is assumed to have a Gaussian shape which peaks at 20 km altitude, with a 1 km full-width-half maximum. (2) The ~~OPAC (Hess et al., 1998) sulphate droplet ("SUSO") aerosol type ,~~ sulfate droplet aerosol type at zero relative humidity from Hess et al. (1998) is assumed to define the aerosol size distribution and optical properties. IMS ~~sulfate aerosol optical depth~~ SAOD has been used in previous studies of the Hunga plume (e.g., Sellitto et al., 2022; Legras et al., 2022; Sellitto et al., 2024). The data is available from the UK Centre for Environmental Data Analysis (CEDA) archive (https://catalogue.ceda.ac.uk/uuid/5aa32fb863a048f0b24c541639cfd990/). Data used here are "L3U" files, i.e., data gridded to 0.25°x0.25° spatial sampling in hourly time intervals.

~~For the comparison with the IMS/IASI SOAD, the ICON-ART SAOD was calculated offline from the mass concentrations of the two soluble modes and their respective mass extinction coefficients derived from Mie calculations for 1130 cm^{-1}.~~

2.4 SAL analysis

The Structure-Amplitude-Location (SAL) method, developed by Wernli et al. (2008, 2009) for validation of modeled and observed precipitation fields, is applied to validate our modeled SO_2 column loadings and sulfate aerosol optical depth (SAOD) against observations. The equation for the calculation of the SAL components are given in Wernli et al. (2008).

The SAL method analyzes the agreement of objects in two-dimensional data fields according to three components: Structure (S), Amplitude (A), and Location (L). S compares modeled and observed normalized objects with respect to their volume. It can have values between -2 (modeled objects are too small and/or too peaked) and 2 (modeled objects are too large and/or too flat). A value of zero indicates a perfect agreement of model and observations with respect to the structure. The evaluation of the domain-averaged relative deviation of the modeled fields from observations is given by the component A. Similar to the S component, A varies between -2 (model underestimates the predicted quantity) and 2 (model overestimates the predicted quantity) with a perfect agreement if A is zero. The agreement in location is given by the component L and is the sum of two steps: first, the agreement between the forecast and observation in terms of the normalized difference between the centers of mass is calculated. Second, the average distance between the center of mass of all objects and the individual objects is derived. Each step can reach values between 0 and 1 so that L in total ranges from 0 to 2 with a perfect forecast with respect to the location at L = 0 (Wernli et al., 2008, 2009).

For the SAL validation of modeled SO_2 column loadings with observations, we used OMPS data. We applied the OMPS detection threshold of 0.2 DU (Li et al., 2017) on both the observational and modeled data field. As the OMPS data is organized

in overpasses, we mapped the data as follows for the SAL comparison: For every overpass, we first chose the corresponding ICON-ART output dataset and checked whether the plume is detected in both fields. If yes, we mapped the overpass area for model and observations onto a 0.25°x0.25° grid. If the plume was detected in the subsequent overpasses as well, we combined these overpasses into one map. In total, we received seven mapped fields containing the plume in the first week after the eruption for the comparison with OMPS ~~: 16 January, 2-4 UTC; 17 January, 2-5 UTC; 18 January, 1-6 UTC; 19 January, 1-8 UTC; 20 January, 1-9 UTC; 21 January, 0-2 UTC; 21 January, 5-11 UTC.~~ (Fig. C1).

For the comparison with the IMS/IASI SOAD, the ICON-ART SAOD was calculated offline from the mass concentration m_l in kg/m^3 of the two soluble modes l and their respective mass extinction coefficients $k_{i,1130\ cm^{-1}}$ derived from Mie calculations for 1130 cm^{-1}:

$$\tau_{1130\ cm^{-1}} = \sum_{i=1}^{z} \sum_{l=1}^{2} m_l \cdot k_{i,1130\ cm^{-1}} \cdot \Delta z_i \tag{1}$$

with z the model level. We performed a ~~similar~~ comparable procedure with ICON-ART SAOD and IMS/IASI SAOD data for the SAL validation of the sulfate mass, similar to the approach used for the SO_2 column loading. The differences to the procedure with the OMPS SO_2 column ~~loadings~~ loading data are that the IMS/IASI data is already mapped to a 0.25°x0.25° grid for each overpasses, and that the background of the SAOD observations is much busier and it is more difficult to distinguish the plume. Therefore, we used a threshold of 0.01 for the SAOD model and observational data and additionally checked whether the SO_2 Hunga plume was available in the same grid cell in the IASI data. In total, twelve mapped fields containing the plume were detected ~~: 15 January, 21 UTC; 16 January, 10-12 UTC; 16 January, 21-23 UTC; 17 January, 11-13 UTC; 17 January, 22 UTC - 18 January 2 UTC; 18 January, 11-14 UTC; 19 January, 0-3 UTC; 19 January, 12-16 UTC; 20 January, 1-4 UTC; 20 January, 13-17 UTC; 21 January, 1-4 UTC; and 21 January, 15-17 UTC.~~ (Fig. C2).

3 Drivers of in-plume chemistry and microphysics

In this section, we ~~want~~ aim to investigate the role of ARI, water vapor, and ash emission on the oxidation of SO_2 and the formation of sulfate aerosols and ash aging.

3.1 Impact of water vapor and SO_2 emissions

Previous ~~works have~~ work has already shown a faster oxidation of SO_2 in the Hunga plume due to the additional emission of water vapor (e.g., Sellitto et al., 2022; Zhu et al., 2022; Asher et al., 2023). Therefore, we focus on the effects of water vapor emission and SO_2 amount on the microphysical developments in the first hours of the plume (i.e., focus on the experiments 1/3xSO_2, noH_2Ochem, Reference) and compare our results to existing studies. Figure 1 shows the temporal mass development of SO_2, sulfate, the water on aerosols, ash, water vapor, and OH~~in all experiments (except the noVolc case)~~.

The co-emission of water vapor accelerates the oxidation of SO_2 and the formation of sulfate aerosols (~~comparing~~ compare 1/3xSO_2 and noH_2Ochem experiments in ~~Figure~~Fig. 1a and b), which agrees with the findings by Zhu et al. (2022). The faster

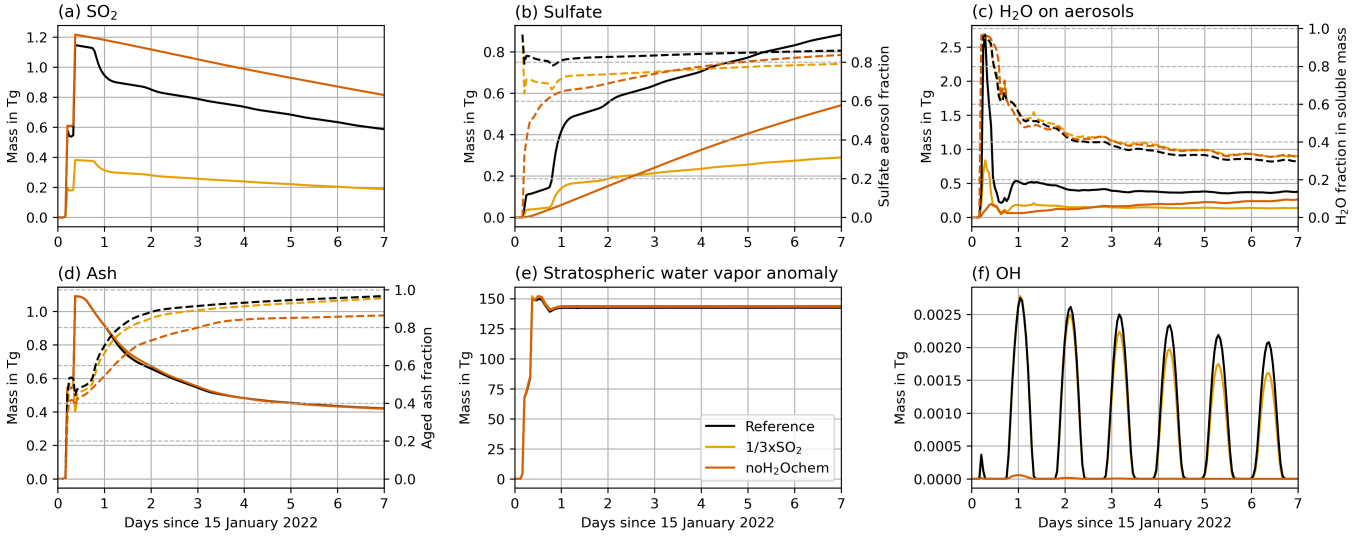

Figure 1. Temporal plume mass development (solid lines, left y-axis) of (a) SO_2, (b) sulfate aerosols plus sulfate on coated ash, (c) liquid water in sulfate aerosols plus liquid water on coated ash, (d) ash, (e) stratospheric water vapor anomaly, and (f) OH for the experiments Reference, 1/3xSO_2, and noH_2Ochem. The dashed lines (right y-axis) indicate fractions of (b) sulfate aerosol mass divided by total sulfate mass, (c) water mass divided by the sum of water and sulfate mass, (d) aged ash mass divided by total ash mass.

SO_2 oxidation in the presence of the water vapor plume is caused by the increase in OH radicals (~~Figure~~Fig. 1f) ~~as a product of~~ produced via water vapor and ozone chemistry in the stratosphere.

All experiments with H_2O contribution to chemistry show a strong reduction of SO_2 in the last quarter of the first day, whereas, the experiment noH_2Ochem reveals a linear decrease (Fig. 1a) within the first week. This strong decrease is due to both the high water vapor concentration in the plume shortly after the emission and the onset of the OH production by photolysis (Fig. 1a and f).

The experiment ~~with~~ 1/~~3 SO~~3xSO_2 ~~emission~~ shows a significantly smaller formation of sulfate, because less SO_2 is available for oxidation (Fig. 1a and b). A larger sulfate formation leads to more water accumulation on aerosols (~~e.g.,~~ compare experiments 1/3xSO_2 and Reference in Fig. 1b and c). The H_2O fraction in soluble mass (Fig. 1c, right y-axis) was calculated as the mass of H_2O in aerosols divided by the mass of H_2O and sulfate in aerosols. The fraction peaks during the first hours when the water vapor concentration ~~was~~ is highest (i.e., during the emission) and decreases over time. Thus, the fraction of sulfate increases in the soluble mixture. The soluble mass after one week ~~was~~ is composed of roughly 2/3 sulfate and 1/3 H_2O with small differences between ~~all experiments including ARI. For experiment noARI, the fraction of H_2O in aerosols is higher (roughly 40%).The reason might be that the plume is transported in lower altitudes in noARI, where the temperatures in the plume are lower and the relative humidity is larger (Figure B1; more on the effect of ARI in section 3.2).~~ the experiments shown in Fig. 1.

Satellite instruments detected ash on the first day after the eruption, however, it is not detectable in the following days~~anymore~~. In the next section, we investigate whether ash played a role on the plume development during the first hours after the eruption and whether aerosol aging, accelerated by the fast SO_2 oxidation, explains why satellites could not detect ash ~~anymore~~ during the further transport.

3.2 Impact of ash and aerosol-radiation interaction

ARI can increase the scattering of sunlight (e.g., Robock, 2000; Timmreck, 2012) and can reduce photolysis in volcanic plumes. Ash aerosols can coagulate with sulfate or provide surfaces for H_2SO_4 condensation, resulting in the aging of volcanic ash and lower amounts of sulfate aerosols. ~~Here, we first~~ In this section, we discuss the role of ash and ARI on the development of the Hunga plume. Therefore, we focus on the experiments Reference, noARI, noCoag, and noAsh in ~~Figure~~Fig. 2, i.e., the experiments with larger SO_2 emission and with volcanic water vapor contribution to chemistry.

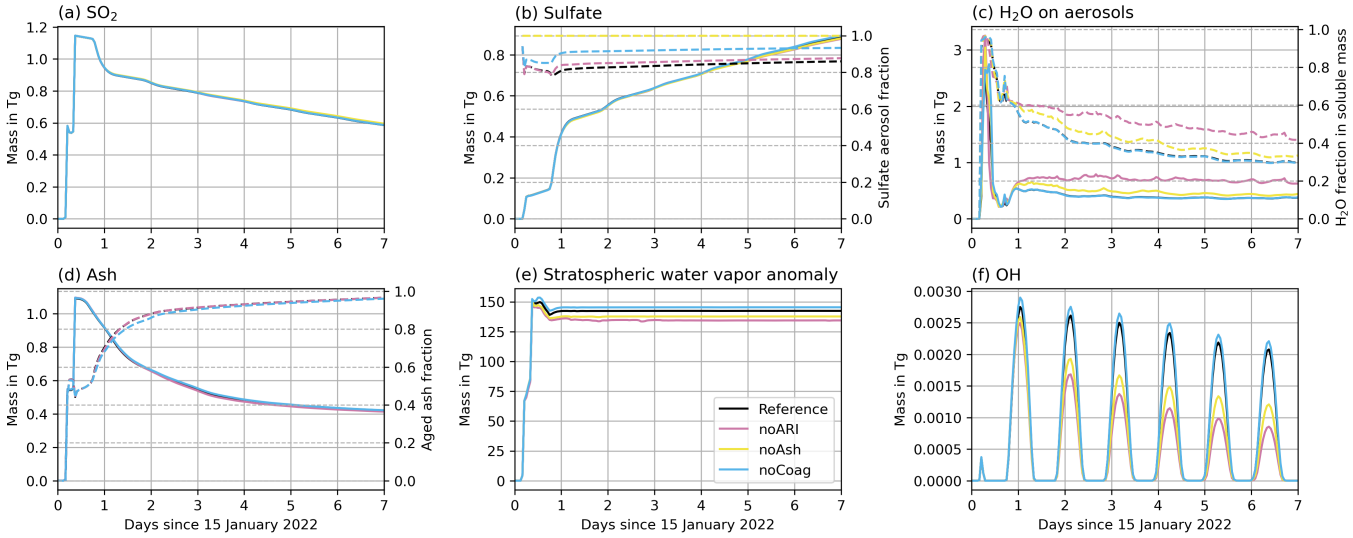

Figure 2. Same as ~~Figure~~Fig. 1, but for the experiments Reference, noARI, noCoag, and noAsh. Note that the curves in a), b), and d) are overlapping.

ARI decreases the oxidation of SO_2 in the Hunga plume only very slightly (~~Figure~~Fig. 2b, compare noARI and Reference). ~~We note that determining~~ Determining the pure effect of the reduction in sunlight on the SO_2 oxidation is difficult to model in a physically consistent way, because ARI causes a lofting of the plume to layers with larger ozone concentrations. A higher concentration of ozone can increase the SO_2 oxidation, which represents an opposed effect to the reduction of sunlight by ARI, i.e., the pure effect of the blocking of sunlight by aerosols might be larger that the ARI effect visible in ~~Figure~~Fig. 2b.

The presence of ash particles in the plume ~~leads to~~ results in a slightly lower fraction of sulfate aerosols relative to the total sulfate mass (dashed lines in ~~Figure~~Fig. 2b, compare Reference and noAsh experiments), because ash particles provide surfaces for H_2SO_4 condensation and coagulation. This leads to aging or coating of the ash, which is a bit faster when more SO_2 is

emitted (dashed lines in ~~Figure~~Fig. 1d, Reference and 1/3xSO_2 experiment). In all experiments, except the noH_2Ochem, more than 90% of the ash mass in the plume is coated after less than 3 days (dashed lines in ~~Figures~~Fig. 1d and 2d). ~~The aging of ash~~ Ash aging is slower without ~~H_2O~~ volcanic water vapor contribution to chemistry (~~Figure~~Fig. 1d dashed line for noH_2Ochem). Nevertheless, more than 80% of the ash is aged after one week in the experiment, despite the smaller oxidation of SO_2. Comparing the curve for the sulfate aerosol fraction of the noH_2Ochem experiment with the curves of the 1/3xSO_2, Reference, and noARI experiments, we can conclude that sulfate tends to form a coating on ash particles rather than creating uniform sulfate particles (~~Figures~~Fig. 1b and 2b). The early aging of ash mainly happens through condensation of soluble components (e.g., sulfate and/or water) rather than coagulation of ash with sulfate aerosols (compare dashed lines for Reference and noCoag in ~~Figure~~Fig. 2d).

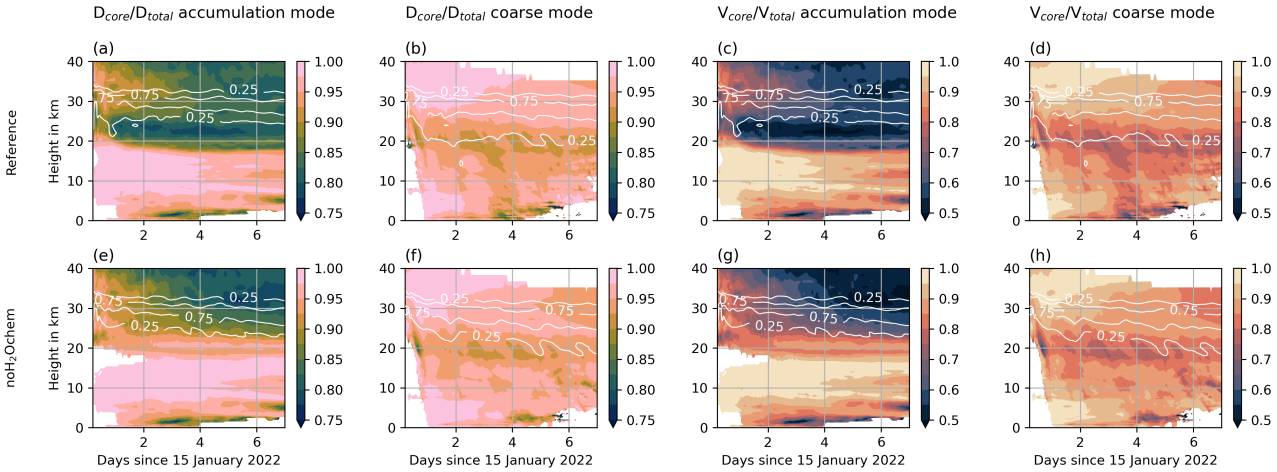

Figure 3. Coating fraction in the Reference experiment (top row) and the noH_2Ochem experiment (bottom row) based on the fraction of core to total particle diameter (first and second column) and based on the fraction of core to total particle volume (third and forth column) in color. The first and third column refer to the mixed accumulation mode and the second and forth column refer to the mixed coarse mode. The white contour lines ~~are~~ refer to the ~~normalized masses~~ fraction of ~~the respective mixed mode per m vertical column~~ maximum aerosol concentrations and indicate the vertical distribution of the plume.

Figure 3 shows the coating fraction ~~with respect to the~~ based on particle diameter (first and second column) and particle volume (third and fourth column) of the mixed accumulation (first and third column) and the coarse (second and forth column) mode for the Reference (top row) and the noH_2Ochem (bottom row) experiment. Besides a larger fraction of aged particles, as discussed before, the coating itself on ash particles also increases with water vapor emission. The differences in coating fraction between the two experiments is largest for the accumulation mode between 20 and 25 km, where the shell makes up about 20% by diameter or about 50% by volume of the particles (compare ~~Figure~~Fig. 3a and e or c and g). For the coarse mode particles, the coating fraction is larger after about three days at the altitude where sedimentation of particles becomes visible, i.e., below 20 km (~~Figure~~Fig. 3b and f or d and h).

Although ~~the aging of ash~~ ash aging is faster when large amounts of water vapor are available in the plume, the coating is not large enough to remove a majority of the ash within the first day as ~~it~~ was proposed by ~~satellites (e.g. Legras et al., 2022)~~satellite observations (e.g., Legras et al., 2022). One reason for the discrepancy between our model results and satellite observations could be that coated ash, which tends to be more spherical compared to the uncoated ash, was interpreted as sulfate by the satellite algorithm. Another reason could be that we miss one or more important aerosol dynamical processes in our current model setup, such as the coagulation of ash with sea salt injected into the stratosphere by the eruption (Colombier et al., 2023) . Sea salt is more hygroscopic than sulfate and might increase the water uptake on aged ash particles, which leads to a faster growth and removal by sedimentation. The neglected activation of ash or the missing wet aggregation in the plume in our model setup might also explain the discrepancy between our simulations and observations. However, the role of sea salt in the Hunga plume on aerosol dynamical processes and the effects of aggregation and activation are beyond the scope of this study and are the topic of another ongoing investigation.

Considering ARI leads to a soluble mass that is composed of roughly 2/3 sulfate and 1/3 H_2O with small differences between the experiments (Fig. 1c and 2c). For experiment noARI, the fraction of H_2O in aerosols is higher (roughly 40%). The reason might be that the plume is transported at lower altitudes in noARI, where the temperatures in the plume are lower and the relative humidity is larger (Fig. B1).

The water vapor development in the plume shows small differences due to ~~aerosol-radiation interaction (Figure~~ARI (Fig. 2e, compare Reference and noARI), which leads to a warming of surrounding air and a lofting of the plume to warmer stratospheric layers (Muser et al., 2020). However, the amount of ash in the Hunga plume is too small to significantly heat the plume and reduce the rate of ice formation in the initial phase of the eruption (~~Figures~~Fig. 1e and 2e). The effect of ARI is discussed in more detail in the following.

Figure 4 shows the mass-averaged height of the water vapor plume in the different experiments in a) and the temperature anomaly of the experiments in b-g). The experiment noARI shows a decrease of more than 3 km within the first week (~~Figure~~Fig. 4a) due to water vapor cooling in the stratosphere (~~Figure~~Fig. 4f). The experiments including ARI also reveal a negative temperature anomaly from about 28 to 33 km coinciding well with the position of the water vapor plume (~~Figure~~Fig. 4b-e and g). However, the descent of the water vapor is reduced (in the noAsh experiment), balanced out (in Reference, noH2Ochem, and 1/3xSO_2 experiments), or even opposed (in the noCoag experiment) after the first day by the warming due to ARI.

All experiments show a steep decrease of the water vapor plume averaged height during the first day (~~Figure~~Fig. 4a). The reasons are (1) a large concentration of water vapor during and in the first hours after the emission leading to strong radiative cooling, (2) the absence of sunlight during the night (emission at 17.00-18.00 and 21.00-22.00 local time), and (3) the strong formation of sulfate starting after the first day.

The reduction ~~of the~~ in descent rate after the first day is due to both sulfate and ash interaction with radiation. Ash contributes by approximately 2/3 (compare Reference and noAsh in ~~Figure~~Fig. 4a) and sulfate contributes by about 1/3 (compare noARI and noAsh in ~~Figure~~Fig. 4a) to the decrease in descent rate.

The experiment noCoag shows the smallest descent rate for the water vapor plume (~~Figure~~Fig. 4a, blue curve) ~~,~~ because coagulation decreases the number concentration of particles and increases the radii. Neglecting this process changes the in-

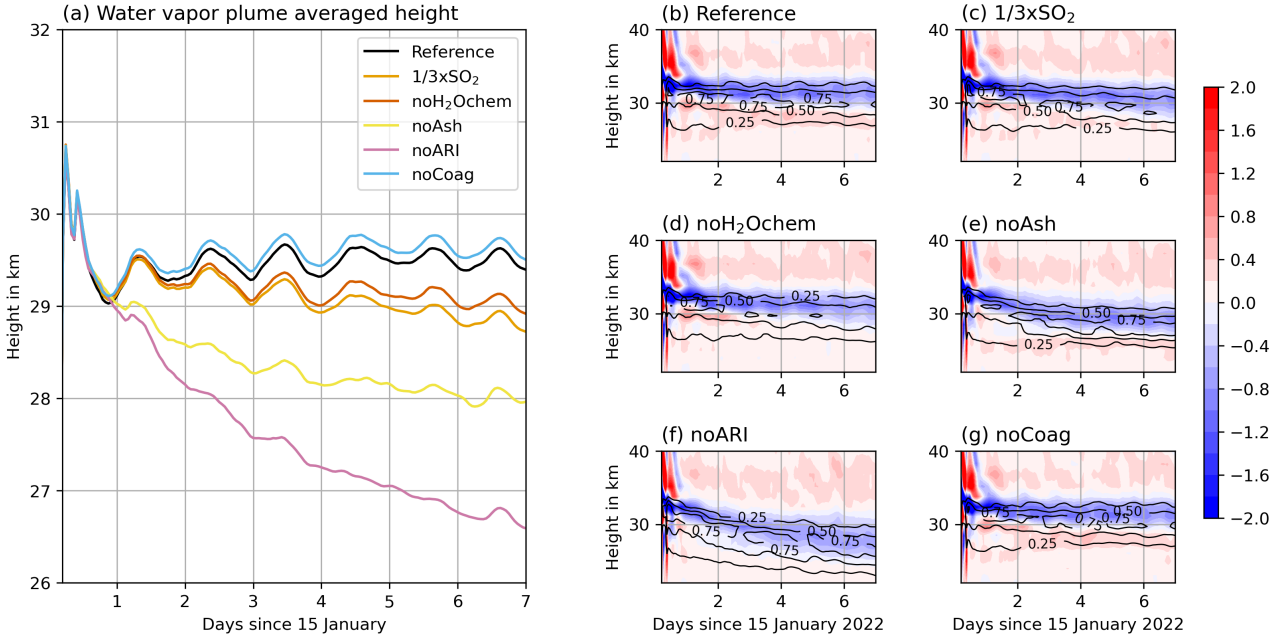

Figure 4. a) Temporal evolution of the mass-averaged water vapor plume height, and b-g) plume temperature anomaly in K in colors and ~~normalized~~ fraction of maximum volcanic water vapor ~~mass per m vertical column~~ concentrations in black contours for the different experiments.

teraction of aerosols with radiation consequently affecting the plume temperatures and lofting. ~~As~~ For particles of the same composition but different size, the smaller particles interact stronger with radiation in the visible range~~,~~. This increases the warming and lofting of the plume in the noCoag case~~is larger~~, which also affects the mass-averaged height of the water vapor plume (~~Figure~~Fig. 4a and g).

Khaykin et al. (2022) found a descent rate of the plume on the order of 200 m per day during the first three weeks in water vapor observations with the Microwave Limb Sounder (MLS; maximum plume top altitudes decreasing from near 30 km between 16 and 19 January to about 26 km between 1 and 10 February). Together with our finding in noARI, we argue that ARI is necessary to reproduce the observed plume descent. However, our simulations with ash seem to underestimate the ash removal, which leads to an overestimation of the radiative warming by aerosols and an underestimation of the water vapor descent. The descent rate of water vapor in the experiment noAsh is closest to the observed descent by Khaykin et al. (2022).

Stenchikov et al. (2024) found a descent from 35 km to 27 km in the first two weeks in model simulations, which is even stronger than in our noAsh experiments. Reasons for the discrepancy to our results are likely to be attributed to differences in the emission assumptions and the lower vertical resolution of the model in Stenchikov et al. (2024). Especially, differences in the vertical emission profile, emission timing, and horizontal emission area affect the concentration of water vapor in the initial phase and, consequently, also the interaction with radiation.

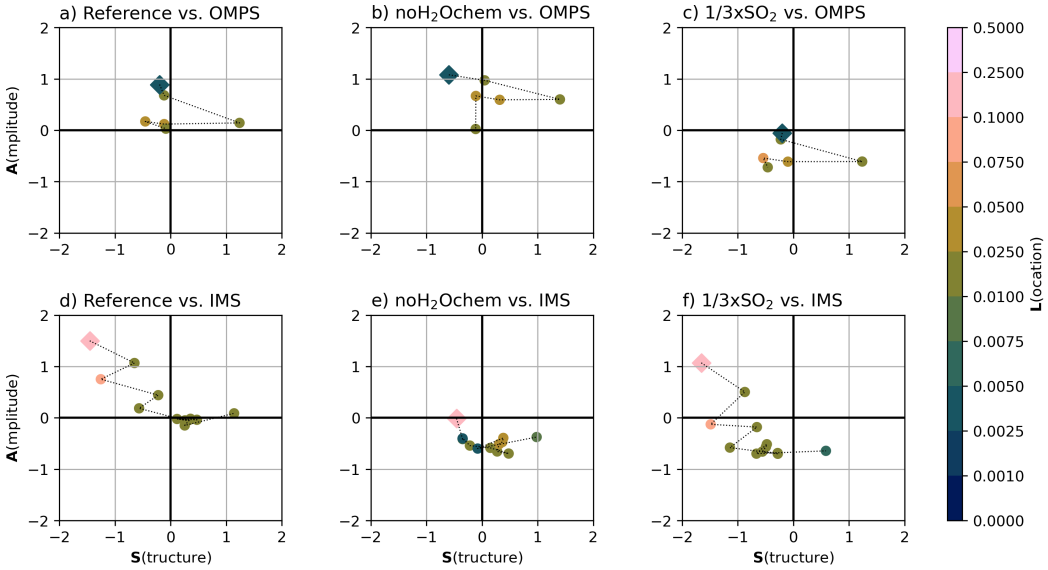

Figure 5. SAL analysis between ICON-ART and OMPS SO_2 column loadings (top, a-c) and between ICON-ART and IMS ~~sulfate AOD~~ SAOD (bottom, d-f) for the experiment Reference (left column), noH_2Ochem (middle column), and 1/3xSO_2 (right column). The structure value is given on the x-axis, the y-axis shows the amplitude value, and the location value is indicated in colours. Each symbol in the plot refers to one comparison date, where the square symbol indicates the first comparison and subsequent comparisons are connected by the dashed line. The corresponding dates and mapped SO_2 column loadings and SOADs are given in ~~section~~Fig. ~~2.4~~C1 and C2.

Positive temperature anomalies arise in all experiments in the first hours after the eruptions above 33 km (~~Figure~~Fig. 4b-g). This is an effect of microphysical processes (mainly ice formation) in the plume during the emission (not shown).

4 Validation of model results

In this section, we ~~will only focus~~ focus only on the experiments Reference, noH_2Ochem, and 1/3xSO_2, as the other experiments show only small differences to the Reference case with respect to the masses of aerosols and SO_2 (~~section~~Sect. 3). These differences are not distinguishable in the comparison to observations (not shown).

4.1 SAL analysis to validate SO_2 oxidation and sulfate formation

We performed an SAL analysis to validate the modeled SO_2 oxidation with OMPS observations (SO_2 column loadings) and modeled sulfate formation with IMS/IASI observations (SAOD). The results are shown in ~~Figure~~Fig. 5 for the experiments Reference (left), noH_2Ochem (middle), and 1/3xSO_2 (right).

The best agreement of model and observations with respect to both SO_2 and sulfate is achieved in the Reference simulation (~~Figure~~Fig. 5a and d). Especially in the latter half of the simulation, all values are close to zero for both SO_2 and sulfate. In

the first days, the amplitude value is around 1 for both compounds, which might indicate an overestimation of the variables by the model. However, during the first days a thick ice and ash plume was visible (e.g., Legras et al., 2022), which might have masked SO_2 and sulfate in the observations. Furthermore, OMPS might have not detected the SO_2 plume well in the first days because of insufficient sampling.

Neglecting the effect of volcanic water vapor on chemistry ~~results in~~ leads to an underestimation of the SO_2 oxidation, i.e., an overestimation of the SO_2 column loadings (~~Figure~~Fig. 5b). Additionally, the SAOD and, thus, the sulfate formation was underestimated by the model in the latter half of the simulation in the noH_2Ochem experiment.

Although the 1/3xSO_2 experiment reveals a reasonable agreement with respect to all SAL components for the SO_2 column loadings in the first half of the simulation, it clearly underestimates the formation of sulfate after the eruption and the SO_2 column loadings in the second half of the simulation (~~Figure~~Fig. 5c and f). This indicates that the SO_2 mass was larger than the initial estimate of 0.4 Tg by Carn et al. (2022) and was approximately two to three times larger ~~(Sellitto et al., 2022, 2024, and Figure 5a)~~ (Sellitto et al., 2022, 2024, and Fig. 5a).

The location values for all experiments are slightly better for SO_2 column loadings than for SAOD ~~,~~ because the SO_2 plume can be more distinctly separated from background SO_2 than is the case for sulfate. Nevertheless, the location values indicate a good agreement between model and observations for all times, both components, and all experiments.

4.2 CALIPSO overpasses to validate transport and composition

We analyzed nine Hunga plume overpasses by the CALIPSO satellite and compared the ATB from CALIOP with the Reference, 1/3xSO_2, and noH_2Ochem experiments as well as the CALIOP depolarization ratio with the spherical fraction ((sulfate mass + aged ash mass) / total aerosol mass) and the sulfate fraction (sulfate mass / total aerosol mass) of the experiments. Figures 6 and 7 show two examples, the other seven overpasses can be found in the Appendix D1-D7.

The overpass from 16 January 2022 at 3:00 UTC indicates two plumes at (1) 15-20 km and (2) 27-30 km (20-30 km for noH_2Ochem) at about 23 to 27°S ~~,~~ in the CALIOP and ICON-ART ATB (~~Figure~~Fig. 6b, d, h, k). The upper signal consists of spherical particles (indicated by the blue-greenish colors in ~~Figure~~Fig. 6c), and it is well reproduced by the aerosol ATB by the ICON-ART experiments Reference and 1/3xSO_2. The ICON-ART spherical and sulfate fractions of the Reference and 1/3xSO_2 indicate that this plume is dominated by spherical particles consisting of both aged ash and sulfate (~~Figure~~Fig. 6e, f, i, and j). For the noH_2Ochem experiment (~~Figure~~Fig. 6k and i) the upper signal reaches lower ~~altitude~~ altitudes and the plume is dominated by non-spherical particles. Thus, without the effect of volcanic water vapor on chemistry the satellite observations can not be reproduced.

The lower signal in the CALIOP ATB most likely originates from ice formed from the Hunga volcanic water vapor ~~,~~ because it is visible in the hydrometeor mixing ratios in all three experiments including volcanic emissions (white contours in ~~Figure~~Fig. 6d, h, and k), but is absent in the experiment without volcanic emission (~~Figure~~Fig. 6g). The CALIOP depolarization ratio further ~~underlines~~ supports that this signal comes from non-spherical particles such as ice or uncoated ash (indicated by reddish colors in ~~Figure~~Fig. 6c).

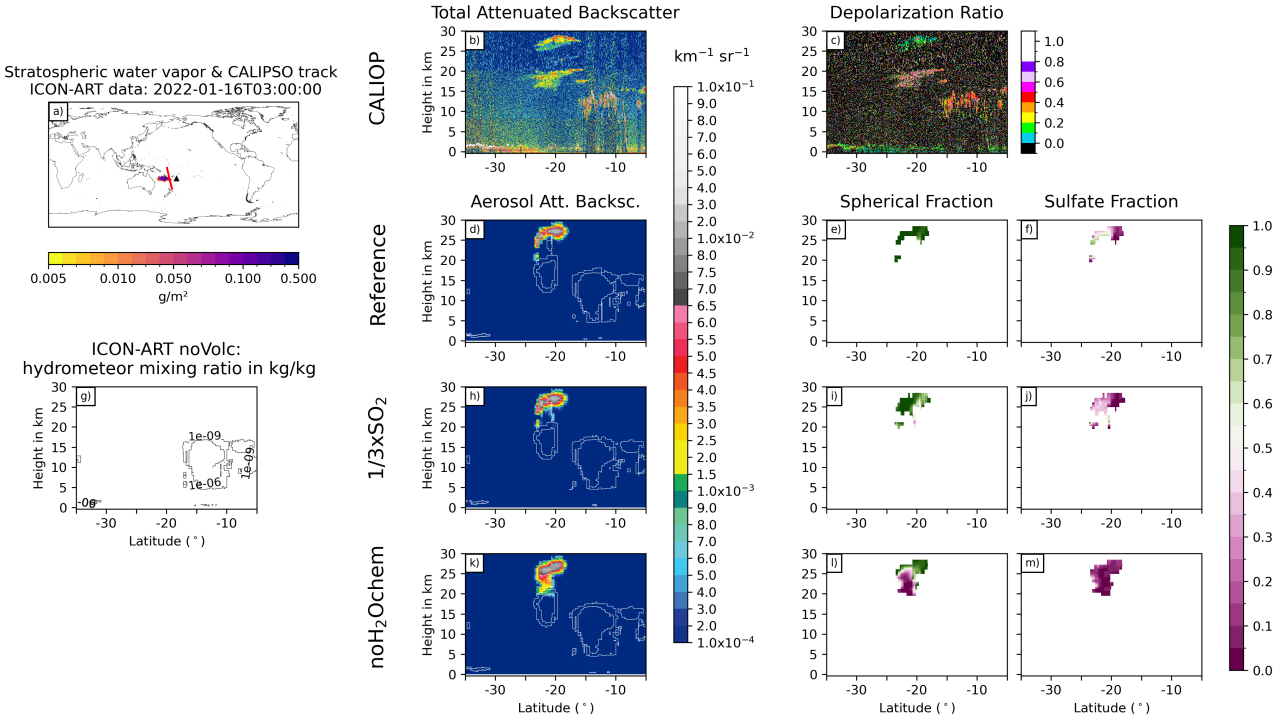

Figure 6. Comparison of ICON-ART and CALIOP for the overpass at 16 January, 2022 at 3:00 UTC. a) shows the stratospheric water vapor column loadings anomaly from ICON-ART with the CALIPSO track as red line and the location of the volcano as a black triangle. The second column compares CALIOP total ATB at 532 nm (b) to ICON-ART aerosol ATB (in colors) for the experiments Reference (d), 1/3xSO_2 (h), and noH_2Ochem (k). The white contours refer to the normalized ~~masses~~ mixing ratios of ICON-ART hydrometeors indicating the position of clouds in the model. Panel (g) refers to the mixing ratio of hydrometeors from the simulation noVolc without volcanic eruption in order to distinguish background meteorological clouds from clouds produced by the volcanic emission of water vapor. The third column shows the CALIOP depolarization ratio (c) and ICON-ART fraction of spherical particle mass (mass of sulfate and aged ash divided by total aerosol mass) for the experiments Reference (e), 1/3xSO_2 (i), and noH_2Ochem (l), respectively. The ~~forth~~ fourth column shows the ICON-ART sulfate fraction defined as the mass of sulfate aerosol divided by the total mass of aerosols for the experiments Reference (f), 1/3xSO_2 (j), and noH_2Ochem (m), respectively.

All ICON-ART experiments (with and without volcanic eruption) indicate hydrometeors in the background north of 17°S and their position agrees reasonably well with the position of the signals in the CALIOP total ATB.

The overpass on 17 January 2022 at 15 UTC shows a layer of non-spherical particles from 5°S to 27°S in the CALIOP measurements at the tropopause (about 18 km), which is only thin at the southern half (less than 3 km thick) and reaches down to 10 km north of 17°S (~~Figure~~Fig. 7b and c). The northern part most likely arises due to hydrometeors in the background and is visible in all experiments (contour lines in ~~Figure~~Fig. 7d, g, h, and k). The southern part, especially south of 20°S, reveals no clouds in the ICON-ART experiments but non-spherical aerosol particles (~~Figure~~Fig. 7d - m). We therefore argue that this

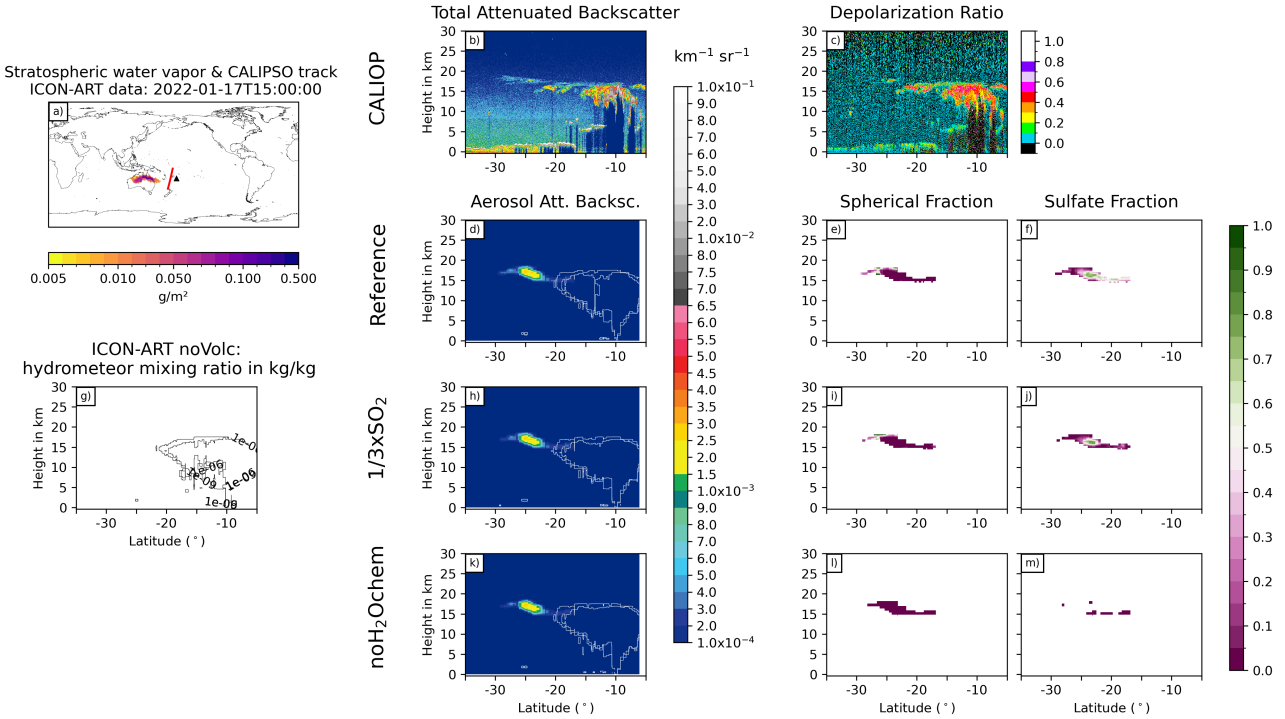

Figure 7. As Fig. 6, but for 17 January, 2022 at 15:00 UTC

signal in the CALIOP total ATB with a ~~rather~~ relatively large depolarization ratio (i.e., non-spherical particles) originates from ~~fresh~~ uncoated ash instead of ice clouds. Nevertheless, the amplitude of the aerosol ATB is slightly overestimated by ICON-ART (~~Figure~~Fig. 7b, d, h, and k).

All in all, the comparison to CALIOP data reveals that parts of the 'missing' ash in satellite data might be hidden due to a strong coating in the presence of volcanic water vapor. However, the simulated aerosol ATB signals tend to overestimate the observed total ATB signals, which agrees with our argumentation in ~~section~~Sect. 3.2 that we miss an important removal processes in our current model setup. Furthermore, the comparison shows that ice particles are present in the plume in model and observations on the first day after the eruption, but the ice was quickly removed, which is in agreement with observations (e.g., Legras et al., 2022; Sellitto et al., 2022).

5 Development of particle sizes

Several measurements show a growth of sulfate particles in the first weeks after the eruption (e.g., Kloss et al., 2022; Asher et al., 2023; Boichu et al., 2023). In this section, we investigate the simulated evolution of the particle size and compare it to previous studies, before we discuss the contribution of the different processes to the particle evolution.

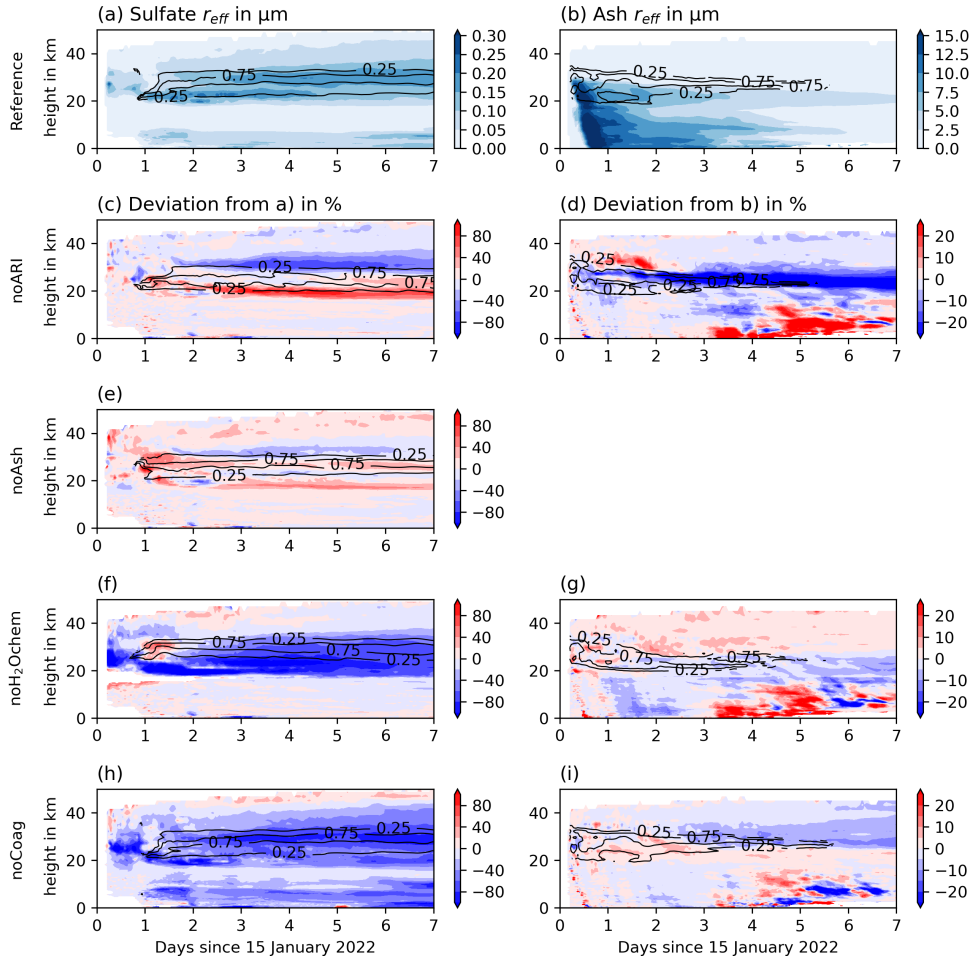

Figure 8. Temporal development of the plume-averaged effective radii for sulfate aerosols (left) and ash aerosols (right) in the Reference experiment (first row), the ~~difference between~~ deviation from Reference for the experiments noARI ~~and Reference~~ (second row), ~~the experiments~~ noASH~~and Reference~~ (third row), ~~the experiments~~ noH$_2$Ochem ~~and Reference~~ (forth row), and ~~the experiments~~ noCoag ~~and Reference~~ (fifth row) in colors. The black contour lines indicate the ~~normalized mass~~ fraction of maximum aerosol concentrations for the sulfate (left column) and ash plume (right column)~~per m vertical column~~, respectively, in order to visualize the vertical distribution of the plume.

Figure 8 shows height-time cross sections of the sulfate and ash effective radii for the Reference experiment (top row) and deviations from Reference for the noARI, noASH, ~~noH2Ochem~~noH$_2$Ochem, and noCoag experiments. The values are horizontally averaged over the entire plume. The sulfate ~~diameter~~ effective radius increases over time during the first week after the eruption by ~~about 2-3 times~~ a factor of about 2 to 3 (Fig. 8a), which has also been found in observations (e.g., Asher et al., 2023; Boichu et al., 2023; Randel et al., 2023). The maximum effective sulfate radius after one week is about 0.35 μm, which ~~is lower than the measured particles sizes of >0.56 μm after seven days in Asher et al. (2023). Boichu et al. (2023) investigated~~

~~the particle sizes in AERONET data and found an increase of the particle size (peak radius) from 0.22 μm to 0.4-0.5 μm within the first week , which is also larger than our simulated radii. Both studies refer to point measurements instead of plume-averaged values, which might explain the discrepancies of model and observations with respect to the absolute values. As the focus of our work lies on the contribution of aerosol processes to the overall plume development during the first week, a direct comparison with point observations will be addressed in future work.~~ agrees well with the value after one week by Stenchikov et al. (2024).

The ash effective radius decreases fast during the first ~~2-3~~ 3 days, because the larger particles sediment faster than smaller ones. After 1 week, ~~ash particles are~~ the ash effective radius is smaller than 4 μm on average ~~.~~ (Fig. 8 left side). Boichu et al. (2023) found particles ~~of 5 μm peak radius~~ with peak radii larger than typical sulfate particle sizes at one AERONET station and argued that these particles might be sulfate coated ash due to the large size. Our results also indicate that some coated ash might be present in the plume (~~section~~Sect. 4.2), however, based on the findings in ~~section~~Sect. 3.2, we argue that the total amount is overestimated by the simulations.

The increase of the sulfate effective radius is mainly caused by coagulation of sulfate particles (Fig. 8h) and would be significantly smaller without volcanic water vapor (~~Figure~~Fig. 8f). The role of coagulation and volcanic water vapor on the development of the ash radius is smaller compared to the sulfate radius evolution (Fig. 8g and i), but still visible. Although we argued in ~~Section~~Sect. 3.1 that ash coagulation with sulfate particles plays a minor role in ash aging, coagulation among ash particles ~~can still contribute~~ still contributes to particle growth.

The differences in the effective radii of the noARI and Reference experiment are mainly caused by plume lofting in the Reference case. The radius is smaller at around 30 km and larger at around 20 km already after two days, when ARI is neglected (Fig. 8c). Thus, ARI results in a slower sedimentation of larger particles and an increase of the particle lifetime. This effect is stronger for ash. Strong negative anomalies are located between 20 and 25 km throughout the entire week, whereas, the radius increases close to the surface after 4.5 days.

When neglecting the emission of ash, the sulfate ~~diameter~~ effective radius slightly increases in most altitudes because no sulfate is taken up by ash (Fig. 8e). However, the amplitudes of the anomalies are smaller compared to the noARI experiments. The negative anomaly at around 30 km after 2 days is most likely an effect of aerosol-radiation interaction.

6 Conclusions

We performed a set of experiments with the ICON-ART modeling system to investigate the role of volcanic water vapor on OH chemistry and the role of ash and ARI in the Hunga plume in the first week after the eruption. A validation with OMPS and IASI data reveals a good agreement with respect to transport, SO_2 depletion, and sulfate formation for the cases including 1.2 Tg of SO_2 emission and the effect of water vapor emission on chemistry (e.g., Reference experiment). The experiments noH_2Ochem and 1/3xSO_2 overestimate and underestimate the depletion of SO_2, respectively. Both underestimate the formation of sulfate. Our main findings are:

- Volcanic water vapor accelerates the depletion of SO_2 and formation of sulfate in the Hunga plume, which is in agreement with observations (e.g., Legras et al., 2022; Asher et al., 2023) and modeling studies (e.g., Zhu et al., 2022). Additionally, our results show that the volcanic water vapor from the Hunga eruption and the resulting enhancement of the OH-chemistry accelerates ash aging and increases the coating on ash. A comparison with CALIOP data indicates that this effect could mask ash in the observations as spherical particles.

- Aerosol aging due to the processes of condensation and coagulation does not explain the rapid loss of ash after the Hunga eruption as observed by satellite instruments. Although some ash might be masked in the observation due to the strong coating, other important processes are likely missing in our setup that enhance particle growth and removal. Possible limitations could be the coagulation with seasalt (Colombier et al., 2023) and subsequent increase in water vapor accumulation on aerosols, a strong wet aggregation in the early plume (ICON-ART only considers coagulation due to Brownian motion), or the activation of aerosols and subsequent washout.

- Water vapor cools the plume and leads to descent of the water vapor plume. However, this is balanced by the warming of the plume due to ARI. A comparison with observed descent rates indicates that in our simulations with ash emission the warming effect due to aerosols might be overestimated as a result of a missing ash removal process.

- The radius development of the sulfate particles is in agreement with observations with respect to the trend (doubling within one week). Our results show that the process of coagulation as well as the volcanic water vapor effect on chemistry is important to explain the growth of the particles in the first week after the eruption.

Our results are affected by assumptions and uncertainties. The umbrella height of the plume was observed between 30-35 km (Gupta et al., 2022). In our setup, we adjusted the emission height in that way that our stratospheric water vapor anomaly is in agreement with observations. A larger emission height, however, also goes along with larger concentrations of ozone and OH, which might have effects on the oxidation of SO_2.

Bruckert et al. (2022) validated ash column loading for the ICON-ART coupled to FPlume against observations for the 2019 Raikoke eruption and found a good agreement. However, the dynamics of the Hunga eruption are very different compared to the 2019 Raikoke eruption because of the submarine setting of the Hunga volcano. Due to the lack of observations on the ash mass we could not validate our ash emissions in this study. However, the values of the total MER are in agreement with the experiments performed by Mastin et al. (2024) with the Plumeria model (Mastin, 2007) when assuming a plume height of 33.7 km.

Finally, we assumed equal emission strength, height, and length of the two eruption phases as simplifications and due to lacking details. These assumptions lie within the uncertainties of the measurements and observations. Nevertheless, deviations from true values can affect the comparison of the transport ~~,~~ but also microphysical plume processes.

Despite the limitations and assumptions of our model setup, our findings highlight the role of volcanic water vapor on the aging of particles and the development of sulfate particles as well as the role of ARI on the descent of the Hunga water vapor plume. Although our study explains the quick loss of ash particles from the plume only to a certain extent, it contributes to future research on the fate of ash after the Hunga eruption.

Code and data availability. The ICON and ART models are open-source and accessible through: ICON partnership (MPI-M; DWD; DKRZ; KIT; C2SM), 2024. ICON release 2024.10. World Data Center for Climate (WDCC) at DKRZ. DOI: https://doi.org/10.35089/WDCC/IconRelease2024.10. The output data from the ICON-ART simulations performed for this study will published at RADAR4KIT after acceptance of the paper.

Author contributions. GAH obtained the funding, initiated and managed the project. JB performed simulations and analyzed the data. CW, GAH, and SC contributed in the discussions of the results. RS prepared and provided the IMS product. JB prepared the paper with significant contributions and comments on the original draft from all authors.

Competing interests. The authors declare that they have no conflict of interest.

Acknowledgements. This research has been funded by the Deutsche Forschungsgemeinschaft (DFG) as part of the Research Unit VolImpact ~~- subproject VolPlume~~ (FOR2820, DFG Grant 398006378) subproject VolPlume (VO 1603/3-2 and HO 5275/4-2). This work used resources of the Deutsches Klimarechenzentrum (DKRZ) granted by its Scientific Steering Committee (WLA) under project ID bb1070. The funding for open-source publication is provided by the DEAL project (https://deal-konsortium.de/en/).

References

Abdelkader, M., Stenchikov, G., Pozzer, A., Tost, H., and Lelieveld, J.: The effect of ash, water vapor, and heterogeneous chemistry on the evolution of a Pinatubo-size volcanic cloud, Atmospheric Chemistry and Physics, 23, 471–500, https://doi.org/10.5194/acp-23-471-2023, 2023.

Asher, E., Todt, M., Rosenlof, K., Thornberry, T., Gao, R.-S., Taha, G., Walter, P., Alvarez, S., Flynn, J., Davis, S. M., Evan, S., Brioude, J., Metzger, J.-M., Hurst, D. F., Hall, E., and Xiong, K.: Unexpectedly rapid aerosol formation in the Hunga Tonga plume, Proceedings of the National Academy of Sciences, 120, e2219547 120, https://doi.org/10.1073/pnas.2219547120, 2023.

Astafyeva, E., Maletckii, B., Mikesell, T. D., Munaibari, E., Ravanelli, M., Coisson, P., Manta, F., and Rolland, L.: The 15 January 2022 Hunga Tonga Eruption History as Inferred From Ionospheric Observations, Geophysical Research Letters, 49, e2022GL098 827, https://doi.org/https://doi.org/10.1029/2022GL098827, 2022.

Baron, A., Chazette, P., Khaykin, S., Payen, G., Marquestaut, N., Bègue, N., and Duflot, V.: Early Evolution of the Stratospheric Aerosol Plume Following the 2022 Hunga Tonga-Hunga Ha'apai Eruption: Lidar Observations From Reunion (21°S, 55°E), Geophysical Research Letters, 50, e2022GL101 751, https://doi.org/https://doi.org/10.1029/2022GL101751, 2023.

Bekki, S.: Oxidation of volcanic SO2: A sink for stratospheric OH and H2O, Geophysical Research Letters, 22, 913–916, https://doi.org/https://doi.org/10.1029/95GL00534, 1995.

Blumstein, D., Chalon, G., Carlier, T., Buil, C., Hebert, P., Maciaszek, T., Ponce, G., Phulpin, T., Tournier, B., Simeoni, D., Astruc, P., Clauss, A., Kayal, G., and Jegou, R.: IASI instrument: technical overview and measured performances, in: Infrared Spaceborne Remote Sensing XII, vol. 5543, pp. 196 – 207, International Society for Optics and Photonics, SPIE, https://doi.org/10.1117/12.560907, 2004.

Boichu, M., Grandin, R., Blarel, L., Torres, B., Derimian, Y., Goloub, P., Brogniez, C., Chiapello, I., Dubovik, O., Mathurin, T., Pascal, N., Patou, M., and Riedi, J.: Growth and Global Persistence of Stratospheric Sulfate Aerosols From the 2022 Hunga Tonga–Hunga Ha'apai Volcanic Eruption, Journal of Geophysical Research: Atmospheres, 128, e2023JD039 010, https://doi.org/https://doi.org/10.1029/2023JD039010, 2023.

Bruckert, J., Hoshyaripour, G. A., Horváth, A., Muser, L. O., Prata, F. J., Hoose, C., and Vogel, B.: Online treatment of eruption dynamics improves the volcanic ash and SO_2 dispersion forecast: case of the 2019 Raikoke eruption, Atmospheric Chemistry and Physics, 22, 3535–3552, https://doi.org/10.5194/acp-22-3535-2022, 2022.

Bruckert, J., Hirsch, L., Horváth, A., Kahn, R. A., Kölling, T., Muser, L. O., Timmreck, C., Vogel, H., Wallis, S., and Hoshyaripour, G. A.: Dispersion and Aging of Volcanic Aerosols After the La Soufrière Eruption in April 2021, Journal of Geophysical Research: Atmospheres, 128, e2022JD037 694, https://doi.org/https://doi.org/10.1029/2022JD037694, 2023.

Carn, S. A., Yang, K., Prata, A. J., and Krotkov, N. A.: Extending the long-term record of volcanic SO2 emissions with the Ozone Mapping and Profiler Suite nadir mapper, Geophysical Research Letters, 42, 925–932, https://doi.org/https://doi.org/10.1002/2014GL062437, 2015.

Carn, S. A., Krotkov, N. A., Fisher, B. L., and Li, C.: Out of the blue: Volcanic SO2 emissions during the 2021–2022 eruptions of Hunga Tonga—Hunga Ha'apai (Tonga), Frontiers in Earth Science, 10, https://doi.org/10.3389/feart.2022.976962, 2022.

Carr, J. L., Horváth, A., Wu, D. L., and Friberg, M. D.: Stereo Plume Height and Motion Retrievals for the Record-Setting Hunga Tonga-Hunga Ha'apai Eruption of 15 January 2022, Geophysical Research Letters, 49, e2022GL098 131, https://doi.org/https://doi.org/10.1029/2022GL098131, 2022.

Clare, M. A., Yeo, I. A., Watson, S., Wysoczanski, R., Seabrook, S., Mackay, K., Hunt, J. E., Lane, E., Talling, P. J., Pope, E., Cronin, S., Ribó, M., Kula, T., Tappin, D., Henrys, S., de Ronde, C., Urlaub, M., Kutterolf, S., Fonua, S., Panuve, S., Veverka, D., Rapp, R.,

Kamalov, V., and Williams, M.: Fast and destructive density currents created by ocean-entering volcanic eruptions, Science, 381, 1085–1092, https://doi.org/10.1126/science.adi3038, 2023.

Colombier, M., Ukstins, I. A., Tegtmeier, S., Scheu, B., Cronin, S. J., Thivet, S., Paredes-Mariño, J., Cimarelli, C., Hess, K.-U., Kula, T., Latu'ila, F. H., and Dingwell, D. B.: Atmosphere injection of sea salts during large explosive submarine volcanic eruptions, Scientific Reports, 13, 14 435, https://doi.org/10.1038/s41598-023-41639-8, 2023.

Doms, G., Förstner, J., Heise, E., Herzog, H.-J., Mironov, D., Raschendorfer, M., Reinhardt, T., Ritter, B., Schrodin, R., Schulz, J.-P., and Vogel, G.: A Description of the Nonhydrostatic Regional COSMO-Model –Part II: Physical Parameterizations, Deutscher Wetterdienst, https://doi.org/10.5676/DWD_pub/nwv/cosmo-doc_5.05_II, 2018.

Folch, A., Costa, A., and Macedonio, G.: FPLUME-1.0: An integral volcanic plume model accounting for ash aggregation, Geoscientific Model Development, 9, 431–450, https://doi.org/10.5194/gmd-9-431-2016, 2016.

Fountoukis, C. and Nenes, A.: ISORROPIA II: a computationally efficient thermodynamic equilibrium model for K^+– Ca^{2+}– Mg^{2+}– NH_4^+– Na^+– SO_4^{2-}– NO_3^-– Cl^-– H_2O aerosols, Atmospheric Chemistry and Physics, 7, 4639–4659, https://doi.org/10.5194/acp-7-4639-2007, 2007.

Giorgetta, M. A., Brokopf, R., Crueger, T., Esch, M., Fiedler, S., Helmert, J., Hohenegger, C., Kornblueh, L., Köhler, M., Manzini, E., Mauritsen, T., Nam, C., Raddatz, T., Rast, S., Reinert, D., Sakradzija, M., Schmidt, H., Schneck, R., Schnur, R., Silvers, L., Wan, H., Zängl, G., and Stevens, B.: ICON-A, the Atmosphere Component of the ICON Earth System Model: I. Model Description, Journal of Advances in Modeling Earth Systems, 10, 1613–1637, https://doi.org/https://doi.org/10.1029/2017MS001242, 2018.

Gouhier, M., Eychenne, J., Azzaoui, N., Guillin, A., Deslandes, M., Poret, M., Costa, A., and Husson, P.: Low efficiency of large volcanic eruptions in transporting very fine ash into the atmosphere , Scientific Reports, 9, 1–12, https://doi.org/10.1038/s41598-019-42489-z, 2019.

Gupta, A. K., Bennartz, R., Fauria, K. E., and Mittal, T.: Eruption chronology of the December 2021 to January 2022 Hunga Tonga-Hunga Ha'apai eruption sequence, Communications Earth & Environment, 3, 314, https://doi.org/10.1038/s43247-022-00606-3, 2022.

Haghighatnasab, M., Kretzschmar, J., Block, K., and Quaas, J.: Impact of Holuhraun volcano aerosols on clouds in cloud-system-resolving simulations, Atmospheric Chemistry and Physics, 22, 8457–8472, https://doi.org/10.5194/acp-22-8457-2022, 2022.

Harvey, N. J., Huntley, N., Dacre, H. F., Goldstein, M., Thomson, D., and Webster, H.: Multi-level emulation of a volcanic ash transport and dispersion model to quantify sensitivity to uncertain parameters, Natural Hazards and Earth System Sciences, 18, 41–43, https://doi.org/10.5194/nhess-18-41-2018, 2018.

Heinze, R., Dipankar, A., Henken, C. C., Moseley, C., Sourdeval, O., Trömel, S., Xie, X., Adamidis, P., Ament, F., Baars, H., Barthlott, C., Behrendt, A., Blahak, U., Bley, S., Brdar, S., Brueck, M., Crewell, S., Deneke, H., Di Girolamo, P., Evaristo, R., Fischer, J., Frank, C., Friederichs, P., Göcke, T., Gorges, K., Hande, L., Hanke, M., Hansen, A., Hege, H.-C., Hoose, C., Jahns, T., Kalthoff, N., Klocke, D., Kneifel, S., Knippertz, P., Kuhn, A., van Laar, T., Macke, A., Maurer, V., Mayer, B., Meyer, C. I., Muppa, S. K., Neggers, R. A. J., Orlandi, E., Pantillon, F., Pospichal, B., Röber, N., Scheck, L., Seifert, A., Seifert, P., Senf, F., Siligam, P., Simmer, C., Steinke, S., Stevens, B., Wapler, K., Weniger, M., Wulfmeyer, V., Zängl, G., Zhang, D., and Quaas, J.: Large-eddy simulations over Germany using ICON: a comprehensive evaluation, Quarterly Journal of the Royal Meteorological Society, 143, 69–100, https://doi.org/https://doi.org/10.1002/qj.2947, 2017.

Hess, M., Koepke, P., and Schult, I.: Optical Properties of Aerosols and Clouds: The Software Package OPAC, Bulletin of the American Meteorological Society, 79, 831 – 844, https://doi.org/10.1175/1520-0477(1998)079<0831:OPOAAC>2.0.CO;2, 1998.

Hogan, R. J. and Bozzo, A.: A Flexible and Efficient Radiation Scheme for the ECMWF Model, Journal of Advances in Modeling Earth Systems, 10, 1990–2008, https://doi.org/https://doi.org/10.1029/2018MS001364, 2018.

Horváth, A., Vadas, S. L., Stephan, C. C., and Buehler, S. A.: One-Minute Resolution GOES-R Observations of Lamb and Gravity Waves Triggered by the Hunga Tonga-Hunga Ha'apai Eruptions on 15 January 2022, Journal of Geophysical Research: Atmospheres, 129, e2023JD039 329, https://doi.org/https://doi.org/10.1029/2023JD039329, 2024.

Hoshyaripour, G. A., Bachmann, V., Förstner, J., Steiner, A., Vogel, H., Wagner, F., Walter, C., and Vogel, B.: Effects of Particle Nonsphericity on Dust Optical Properties in a Forecast System: Implications for Model-Observation Comparison, Journal of Geophysical Research: Atmospheres, 124, 7164–7178, https://doi.org/https://doi.org/10.1029/2018JD030228, 2019.

Khaykin, S., Podglajen, A., Ploeger, F., Grooß, J.-U., Tence, F., Bekki, S., Khlopenkov, K., Bedka, K., Rieger, L., Baron, A., Godin-Beekmann, S., Legras, B., Sellitto, P., Sakai, T., Barnes, J., Uchino, O., Morino, I., Nagai, T., Wing, R., Baumgarten, G., Gerding, M., Duflot, V., Payen, G., Jumelet, J., Querel, R., Liley, B., Bourassa, A., Clouser, B., Feofilov, A., Hauchecorne, A., and Ravetta, F.: Global perturbation of stratospheric water and aerosol burden by Hunga eruption, Communications Earth & Environment, 3, 316, https://doi.org/10.1038/s43247-022-00652-x, 2022.

Kloss, C., Sellitto, P., Renard, J.-B., Baron, A., Bègue, N., Legras, B., Berthet, G., Briaud, E., Carboni, E., Duchamp, C., Duflot, V., Jacquet, P., Marquestaut, N., Metzger, J.-M., Payen, G., Ranaivombola, M., Roberts, T., Siddans, R., and Jégou, F.: Aerosol Characterization of the Stratospheric Plume From the Volcanic Eruption at Hunga Tonga 15 January 2022, Geophysical Research Letters, 49, e2022GL099 394, https://doi.org/https://doi.org/10.1029/2022GL099394, 2022.

LeGrande, A. N., Tsigaridis, K., and Bauer, S. E.: Role of atmospheric chemistry in the climate impacts of stratospheric volcanic injections, Nature Geoscience, 9, 652–655, https://doi.org/10.1038/ngeo2771, 2016.

Legras, B., Duchamp, C., Sellitto, P., Podglajen, A., Carboni, E., Siddans, R., Grooß, J.-U., Khaykin, S., and Ploeger, F.: The evolution and dynamics of the Hunga Tonga–Hunga Ha'apai sulfate aerosol plume in the stratosphere, Atmospheric Chemistry and Physics, 22, 14 957–14 970, https://doi.org/10.5194/acp-22-14957-2022, 2022.

Li, C., Krotkov, N. A., Carn, S., Zhang, Y., Spurr, R. J. D., and Joiner, J.: New-generation NASA Aura Ozone Monitoring Instrument (OMI) volcanic SO_2 dataset: algorithm description, initial results, and continuation with the Suomi-NPP Ozone Mapping and Profiler Suite (OMPS), Atmospheric Measurement Techniques, 10, 445–458, https://doi.org/10.5194/amt-10-445-2017, 2017.

Malavelle, F. F., Haywood, J. M., Jones, A., Gettelman, A., Clarisse, L., Bauduin, S., Allan, R. P., Karset, I. H. H., Kristjánsson, J. E., Oreopoulos, L., Cho, N., Lee, D., Bellouin, N., Boucher, O., Grosvenor, D. P., Carslaw, K. S., Dhomse, S., Mann, G. W., Schmidt, A., Coe, H., Hartley, M. E., Dalvi, M., Hill, A. A., Johnson, B. T., Johnson, C. E., Knight, J. R., O'Connor, F. M., Partridge, D. G., Stier, P., Myhre, G., Platnick, S., Stephens, G. L., Takahashi, H., and Thordarson, T.: Strong constraints on aerosol–cloud interactions from volcanic eruptions, Nature, 546, 485–491, https://doi.org/10.1038/nature22974, 2017.

Mastin, L. G.: A user-friendly one-dimensional model for wet volcanic plumes, Geochemistry, Geophysics, Geosystems, 8, https://doi.org/https://doi.org/10.1029/2006GC001455, 2007.

Mastin, L. G., Van Eaton, A. R., and Cronin, S. J.: Did steam boost the height and growth rate of the giant Hunga eruption plume?, Bulletin of Volcanology, 86, 64, https://doi.org/10.1007/s00445-024-01749-1, 2024.

Matoza, R. S., Fee, D., Assink, J. D., Iezzi, A. M., Green, D. N., Kim, K., Toney, L., Lecocq, T., Krishnamoorthy, S., Lalande, J.-M., Nishida, K., Gee, K. L., Haney, M. M., Ortiz, H. D., Brissaud, Q., Martire, L., Rolland, L., Vergados, P., Nippress, A., Park, J., Shani-Kadmiel, S., Witsil, A., Arrowsmith, S., Caudron, C., Watada, S., Perttu, A. B., Taisne, B., Mialle, P., Pichon, A. L., Vergoz, J., Hupe, P., Blom, P. S., Waxler, R., Angelis, S. D., Snively, J. B., Ringler, A. T., Anthony, R. E., Jolly, A. D., Kilgour, G., Averbuch, G., Ripepe, M., Ichihara, M.,

Arciniega-Ceballos, A., Astafyeva, E., Ceranna, L., Cevuard, S., Che, I.-Y., Negri, R. D., Ebeling, C. W., Evers, L. G., Franco-Marin, L. E., Gabrielson, T. B., Hafner, K., Harrison, R. G., Komjathy, A., Lacanna, G., Lyons, J., Macpherson, K. A., Marchetti, E., McKee, K. F., Mellors, R. J., Mendo-Pérez, G., Mikesell, T. D., Munaibari, E., Oyola-Merced, M., Park, I., Pilger, C., Ramos, C., Ruiz, M. C., Sabatini, R., Schwaiger, H. F., Tailpied, D., Talmadge, C., Vidot, J., Webster, J., and Wilson, D. C.: Atmospheric waves and global seismoacoustic observations of the January 2022 Hunga eruption, Tonga, Science, 377, 95–100, https://doi.org/10.1126/science.abo7063, 2022.

McLinden, C. A., Olsen, S. C., Hannegan, B., Wild, O., Prather, M. J., and Sundet, J.: Stratospheric ozone in 3-D models: A simple chemistry and the cross-tropopause flux, Journal of Geophysical Research: Atmospheres, 105, 14 653–14 665, https://doi.org/https://doi.org/10.1029/2000JD900124, 2000.

Millán, L., Santee, M. L., Lambert, A., Livesey, N. J., Werner, F., Schwartz, M. J., Pumphrey, H. C., Manney, G. L., Wang, Y., Su, H., Wu, L., Read, W. G., and Froidevaux, L.: The Hunga Tonga-Hunga Ha'apai Hydration of the Stratosphere, Geophysical Research Letters, 49, e2022GL099 381, https://doi.org/https://doi.org/10.1029/2022GL099381, 2022.

Muser, L. O., Hoshyaripour, G. A., Bruckert, J., Horváth, A., Malinina, E., Wallis, S., Prata, F. J., Rozanov, A., von Savigny, C., Vogel, H., and Vogel, B.: Particle aging and aerosol–radiation interaction affect volcanic plume dispersion: evidence from the Raikoke 2019 eruption, Atmospheric Chemistry and Physics, 20, 15 015–15 036, https://doi.org/10.5194/acp-20-15015-2020, 2020.

Niemeier, U., Timmreck, C., Graf, H.-F., Kinne, S., Rast, S., and Self, S.: Initial fate of fine ash and sulfur from large volcanic eruptions, Atmospheric Chemistry and Physics, 9, 9043–9057, https://doi.org/10.5194/acp-9-9043-2009, 2009.

Niemeier, U., Wallis, S., Timmreck, C., van Pham, T., and von Savigny, C.: How the Hunga Tonga—Hunga Ha'apai Water Vapor Cloud Impacts Its Transport Through the Stratosphere: Dynamical and Radiative Effects, Geophysical Research Letters, 50, e2023GL106 482, https://doi.org/https://doi.org/10.1029/2023GL106482, 2023.

Podglajen, A., Le Pichon, A., Garcia, R. F., Gérier, S., Millet, C., Bedka, K., Khlopenkov, K., Khaykin, S., and Hertzog, A.: Stratospheric Balloon Observations of Infrasound Waves From the 15 January 2022 Hunga Eruption, Tonga, Geophysical Research Letters, 49, e2022GL100 833, https://doi.org/https://doi.org/10.1029/2022GL100833, 2022.

Prill, F., Reinert, D., Rieger, D., and Zängl, G.: ICON Tutorial – Working with the ICON Model, Deutscher Wetterdienst, https://doi.org/10.5676/DWD_pub/nwv/icon_tutorial2023, 2023.

Proud, S. R., Prata, A. T., and Schmauß, S.: The January 2022 eruption of Hunga Tonga-Hunga Ha'apai volcano reached the mesosphere, Science, 378, 554–557, https://doi.org/10.1126/science.abo4076, 2022.

Purkis, S. J., Ward, S. N., Fitzpatrick, N. M., Garvin, J. B., Slayback, D., Cronin, S. J., Palaseanu-Lovejoy, M., and Dempsey, A.: The 2022 Hunga-Tonga megatsunami: Near-field simulation of a once-in-a-century event, Science Advances, 9, eadf5493, https://doi.org/10.1126/sciadv.adf5493, 2023.

Randel, W. J., Johnston, B. R., Braun, J. J., Sokolovskiy, S., Vömel, H., Podglajen, A., and Legras, B.: Stratospheric Water Vapor from the Hunga Tonga–Hunga Ha'apai Volcanic Eruption Deduced from COSMIC-2 Radio Occultation, Remote Sensing, 15, https://doi.org/10.3390/rs15082167, 2023.

Rieger, D., Bangert, M., Bischoff-Gauss, I., Förstner, J., Lundgren, K., Reinert, D., Schröter, J., Vogel, H., Zängl, G., Ruhnke, R., and Vogel, B.: ICON-ART 1.0 - A new online-coupled model system from the global to regional scale, Geoscientific Model Development, 8, 1659–1676, https://doi.org/10.5194/gmd-8-1659-2015, 2015.

Riemer, N.: Numerische Simulationen zur Wirkung des Aerosols auf die troposphärische Chemie und die Sichtweite, Ph.D. thesis, https://doi.org/10.5445/IR/2212002, 2002.

Robock, A.: Volcanic Eruptions and Climate, Reviews of Geophysics, 38, 191–219, 2000.

Rodgers, C. D.: Inverse methods for atmospheric sounding: theory and practice, vol. 2, World scientific, 2000.

Saunders, R., Hocking, J., Rundle, D., Rayer, P., Havemann, S., Matricardi, M., Geer, A., Lupu, C., Brunel, P., and Vidot, J.: RTTOV-12 Science and Validation Report, Tech. Rep. Doc ID : NWPSAF-MO-TV-41,Version 1.0, Date : 16/02/2017, 2017.

Scollo, S., Folch, A., and Costa, A.: A parametric and comparative study of different tephra fallout models, Journal of Volcanology and Geothermal Research, 176, 199–211, https://doi.org/10.1016/j.jvolgeores.2008.04.002, 2008.

Sellitto, P., Podglajen, A., Belhadji, R., Boichu, M., Carboni, E., Cuesta, J., Duchamp, C., Kloss, C., Siddans, R., Bègue, N., Blarel, L., Jegou, F., Khaykin, S., Renard, J.-B., and Legras, B.: The unexpected radiative impact of the Hunga Tonga eruption of 15th January 2022, Communications Earth & Environment, 3, 288, https://doi.org/10.1038/s43247-022-00618-z, 2022.

Sellitto, P., Siddans, R., Belhadji, R., Carboni, E., Legras, B., Podglajen, A., Duchamp, C., and Kerridge, B.: Observing the SO2 and Sulfate Aerosol Plumes From the 2022 Hunga Eruption With the Infrared Atmospheric Sounding Interferometer (IASI), Geophysical Research Letters, 51, e2023GL105 565, https://doi.org/https://doi.org/10.1029/2023GL105565, 2024.

Siddans, R.: Water Vapour CCI: Algorithm Theoretical Basis Document (ATBD) Part 2 - IMS L2 Product version 2.0, Tech. rep., https://climate.esa.int/documents/2497/Water_Vapour_CCI_D2.2_ATBD_Part2-IMS_L2_product_v2.0.pdf, 21 November, 2023, 2023.

Sioris, C. E., Zou, J., McElroy, C. T., Boone, C. D., Sheese, P. E., and Bernath, P. F.: Water vapour variability in the high-latitude upper troposphere – Part 2: Impact of volcanic eruptions, Atmospheric Chemistry and Physics, 16, 2207–2219, https://doi.org/10.5194/acp-16-2207-2016, 2016.

Stenchikov, G., Ukhov, A., Osipov, S., Ahmadov, R., Grell, G., Cady-Pereira, K., Mlawer, E., and Iacono, M.: How Does a Pinatubo-Size Volcanic Cloud Reach the Middle Stratosphere?, Journal of Geophysical Research: Atmospheres, 126, e2020JD033 829, https://doi.org/https://doi.org/10.1029/2020JD033829, 2021.

Stenchikov, G., Ukhov, A., and Osipov, S.: Modeling the Direct Radiative Forcing and Climate Impacts of the 2022 Hunga Volcano Explosion, https://doi.org/10.22541/essoar.172070583.36131358/v1, in review, 2024.

Suzuki, T.: A Theoretical Model for Dispersion of Tephra, Arc Volcanism: Physics and Tectonics, pp. 95–113, 1983.

Taha, G., Loughman, R., Colarco, P. R., Zhu, T., Thomason, L. W., and Jaross, G.: Tracking the 2022 Hunga Tonga-Hunga Ha'apai Aerosol Cloud in the Upper and Middle Stratosphere Using Space-Based Observations, Geophysical Research Letters, 49, e2022GL100 091, https://doi.org/https://doi.org/10.1029/2022GL100091, 2022.

Timmreck, C.: Modeling the climatic effects of large explosive volcanic eruptions, Wiley Interdisciplinary Reviews: Climate Change, 3, 545–564, https://doi.org/10.1002/wcc.192, 2012.

Ukhov, A., Stenchikov, G., Osipov, S., Krotkov, N., Gorkavyi, N., Li, C., Dubovik, O., and Lopatin, A.: Inverse Modeling of the Initial Stage of the 1991 Pinatubo Volcanic Cloud Accounting for Radiative Feedback of Volcanic Ash, Journal of Geophysical Research: Atmospheres, 128, e2022JD038 446, https://doi.org/https://doi.org/10.1029/2022JD038446, 2023.

Vömel, H., Evan, S., and Tully, M.: Water vapor injection into the stratosphere by Hunga Tonga-Hunga Ha'apai, Science, 377, 1444–1447, https://doi.org/10.1126/science.abq2299, 2022.

Weimer, M., Schröter, J., Eckstein, J., Deetz, K., Neumaier, M., Fischbeck, G., Hu, L., Millet, D. B., Rieger, D., Vogel, H., Vogel, B., Reddmann, T., Kirner, O., Ruhnke, R., and Braesicke, P.: An emission module for ICON-ART 2.0: Implementation and simulations of acetone, Geoscientific Model Development, 10, 2471–2494, https://doi.org/10.5194/gmd-10-2471-2017, 2017.

Wernli, H., Paulat, M., Hagen, M., and Frei, C.: SAL - A Novel Quality Measure for the Verification of Quantitative Precipitation Forecasts, Monthly Weather Review, 136, 4470 – 4487, https://doi.org/10.1175/2008MWR2415.1, 2008.

Wernli, H., Hofmann, C., and Zimmer, M.: Spatial Forecast Verification Methods Intercomparison Project: Application of the SAL Technique, Weather and Forecasting, 24, 1472 – 1484, https://doi.org/10.1175/2009WAF2222271.1, 2009.

Winker, D. M., Vaughan, M. A., Omar, A., Hu, Y., Powell, K. A., Liu, Z., Hunt, W. H., and Young, S. A.: Overview of the CALIPSO Mission and CALIOP Data Processing Algorithms, Journal of Atmospheric and Oceanic Technology, 26, 2310 – 2323, https://doi.org/10.1175/2009JTECHA1281.1, 2009.

Wright, C. J., Hindley, N. P., Alexander, M. J., Barlow, M., Hoffmann, L., Mitchell, C. N., Prata, F., Bouillon, M., Carstens, J., Clerbaux, C., Osprey, S. M., Powell, N., Randall, C. E., and Yue, J.: Surface-to-space atmospheric waves from Hunga Tonga–Hunga Ha'apai eruption, Nature, 609, 741–746, https://doi.org/10.1038/s41586-022-05012-5, 2022.

Xu, J., Li, D., Bai, Z., Tao, M., and Bian, J.: Large Amounts of Water Vapor Were Injected into the Stratosphere by the Hunga Tonga–Hunga Ha'apai Volcano Eruption, Atmosphere, 13, https://doi.org/10.3390/atmos13060912, 2022.

Zängl, G., Reinert, D., Rípodas, P., and Baldauf, M.: The ICON (ICOsahedral Non-hydrostatic) modelling framework of DWD and MPI-M: Description of the non-hydrostatic dynamical core, Quarterly Journal of the Royal Meteorological Society, 141, 563–579, https://doi.org/10.1002/qj.2378, 2015.

Zhu, Y., Toon, O. B., Jensen, E. J., Bardeen, C. G., Mills, M. J., Tolbert, M. A., Yu, P., and Woods, S.: Persisting volcanic ash particles impact stratospheric SO2 lifetime and aerosol optical properties, Nature Communications, 11, 1–11, https://doi.org/10.1038/s41467-020-18352-5, 2020.

Zhu, Y., Bardeen, C. G., Tilmes, S., Mills, M. J., Wang, X., Harvey, V. L., Taha, G., Kinnison, D., Portmann, R. W., Yu, P., Zosenlof, K. H., Avery, M., Kloss, C., Li, C., Glanville, A. S., Millán, L., Deshler, T., Krotkov, N., and Toon, O. B.: Perturbations in stratospheric aerosol evolution due to the water-rich plume of the 2022 Hunga-Tonga eruption, Communications Earth & Environment, 3, 248, https://doi.org/10.1038/s43247-022-00580-w, 2022.

Appendix A: Emission profile and vertical profiles for different components

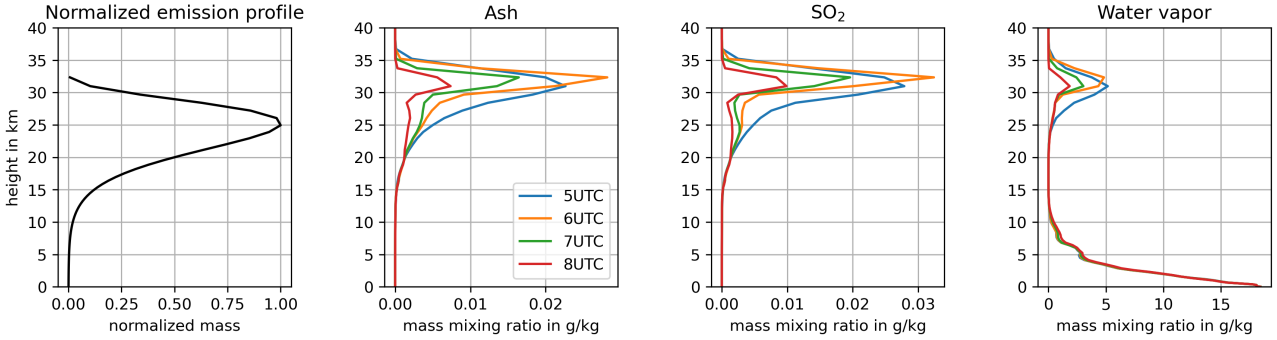

Figure A1. Emission profile (a) and vertical mass mixing ratio profiles one (blue), two (orange), three (green), and four (red) hours after the beginning of the first emission phase for b) ash, c) SO_3, and d) water vapor.

Appendix B: Temperature and humidity in aerosol plume

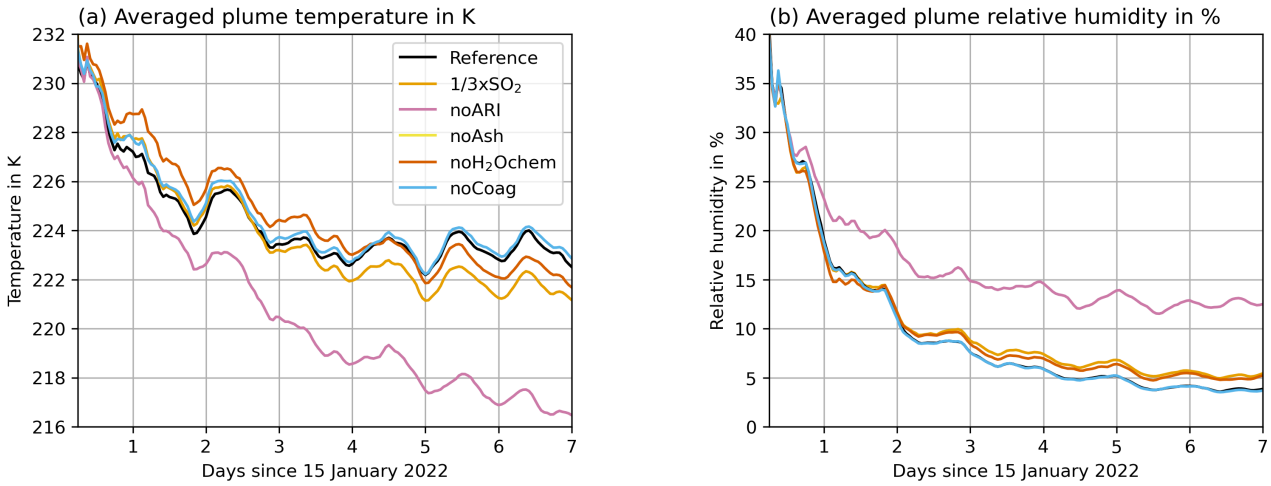

Figure B1. Aerosol-plume averaged a) temperatures in K and b) specific humidity in % in all experiments including the volcanic eruption ~~experiments~~ to explain the difference in the water uptake.

Appendix C: Additional plots for SO_2 and sulfate comparisons

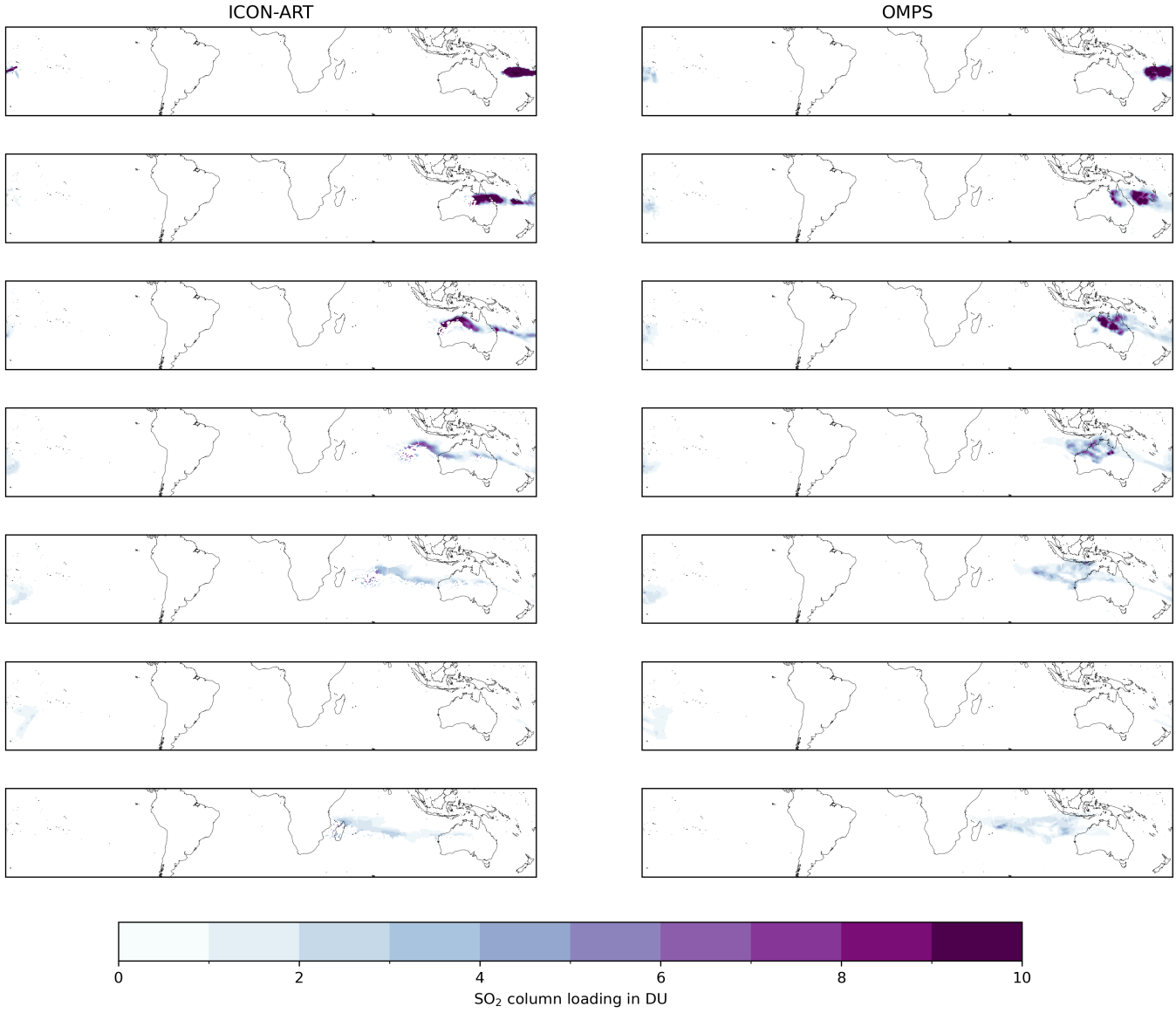

Figure C1. Comparison of the ICON-ART (left) and OMPS (right) SO_2 column loadings in DU for all detected overpasses. The rows from top to bottom refer to the following dates: 16 January, ~~2-4~~2:00-4:00 UTC; 17 January, ~~2-5~~2:00-5:00 UTC; 18 January, ~~1-6~~ 1:00-6:00 UTC; 19 January, ~~1-8~~1:00-8:00 UTC; 20 January, ~~1-9~~ 1:00-9:00 UTC; 21 January, ~~0-2~~0:00-2:00 UTC; and 21 January, ~~5-11~~5:00-11:00 UTC.

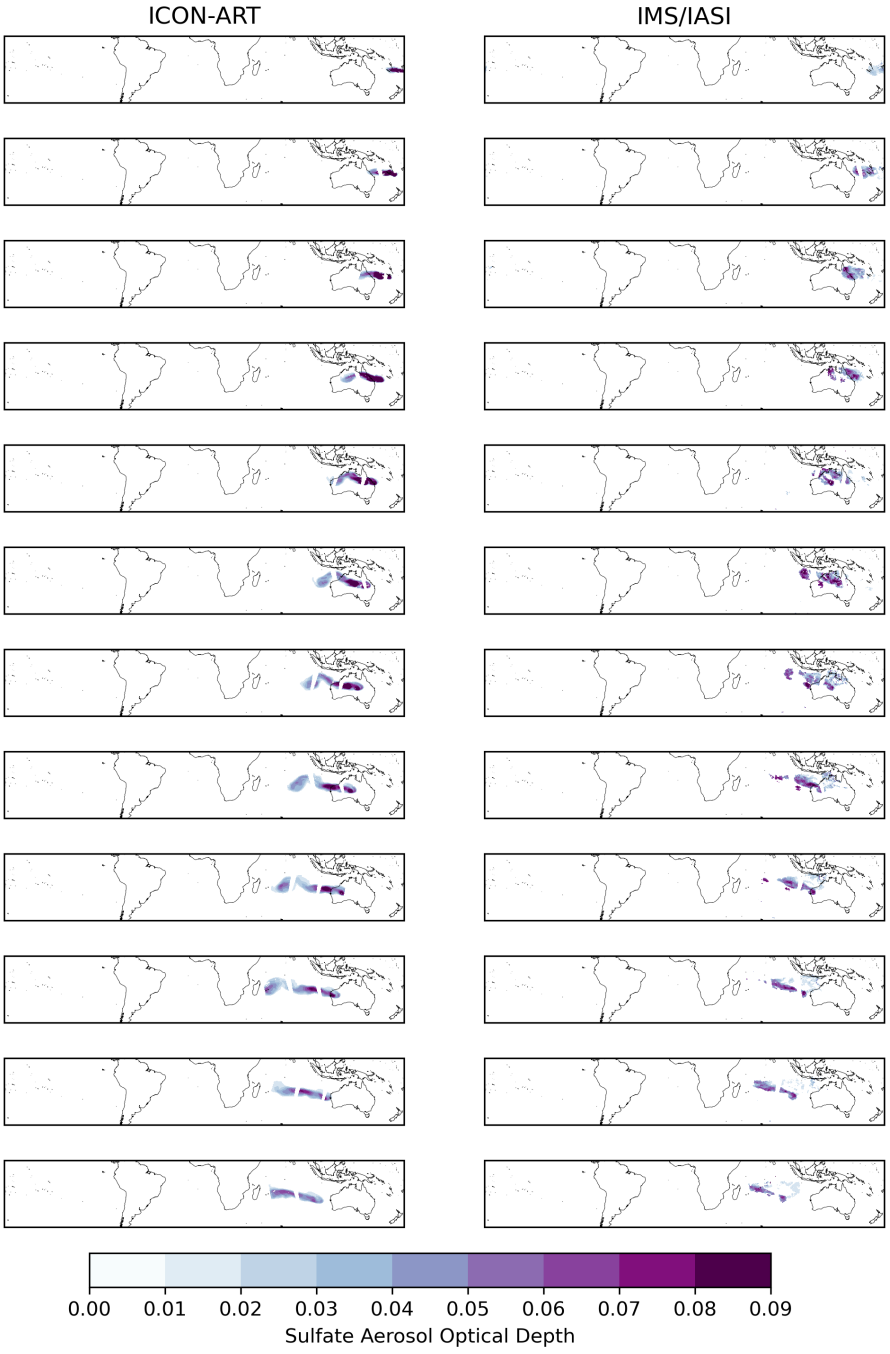

Figure C2. Comparison of the ICON-ART (left) and IMS/IASI (right) SAOD for all detected overpasses. The rows from top to bottom refer to the following dates: 15 January, 21:00 UTC; 16 January, ~~10-12~~10:00-12:00 UTC; 16 January, ~~21-23~~21:00-23:00 UTC; 17 January, ~~11-13~~11:00-13:00 UTC; 17 January, 22:00 UTC - 18 January 2:00 UTC; 18 January, ~~11-14~~11:00-14:00 UTC; 19 January, ~~0-3~~0:00-3:00 UTC; 19 January, ~~12-16~~12:00-16:00 UTC; 20 January, ~~1-4~~1:00-4:00 UTC; 20 January, ~~13-17~~13:00-17:00 UTC; 21 January, ~~1-4~~1:00-4:00 UTC; and 21 January, ~~15-17~~15:00-17:00 UTC.

Appendix D: CALIPSO overpass

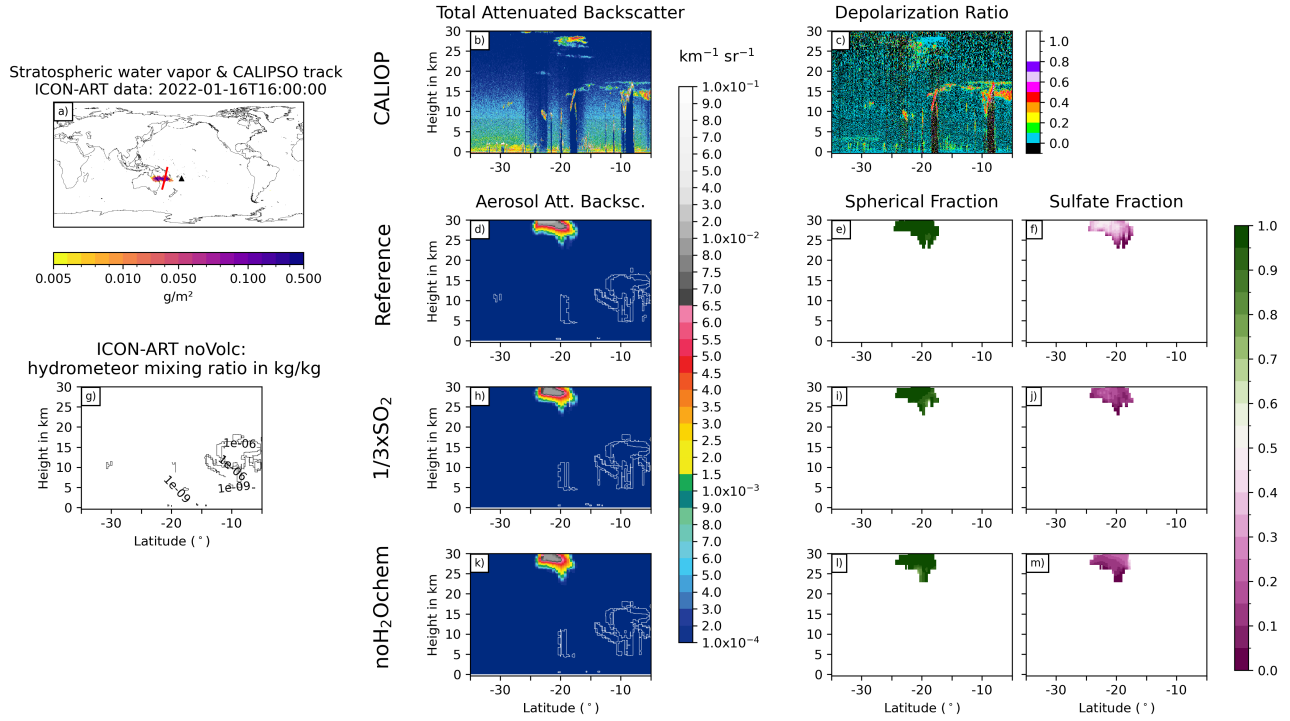

Figure D1. As Fig. 6, but for 16 January, 2022 at 16:00 UTC

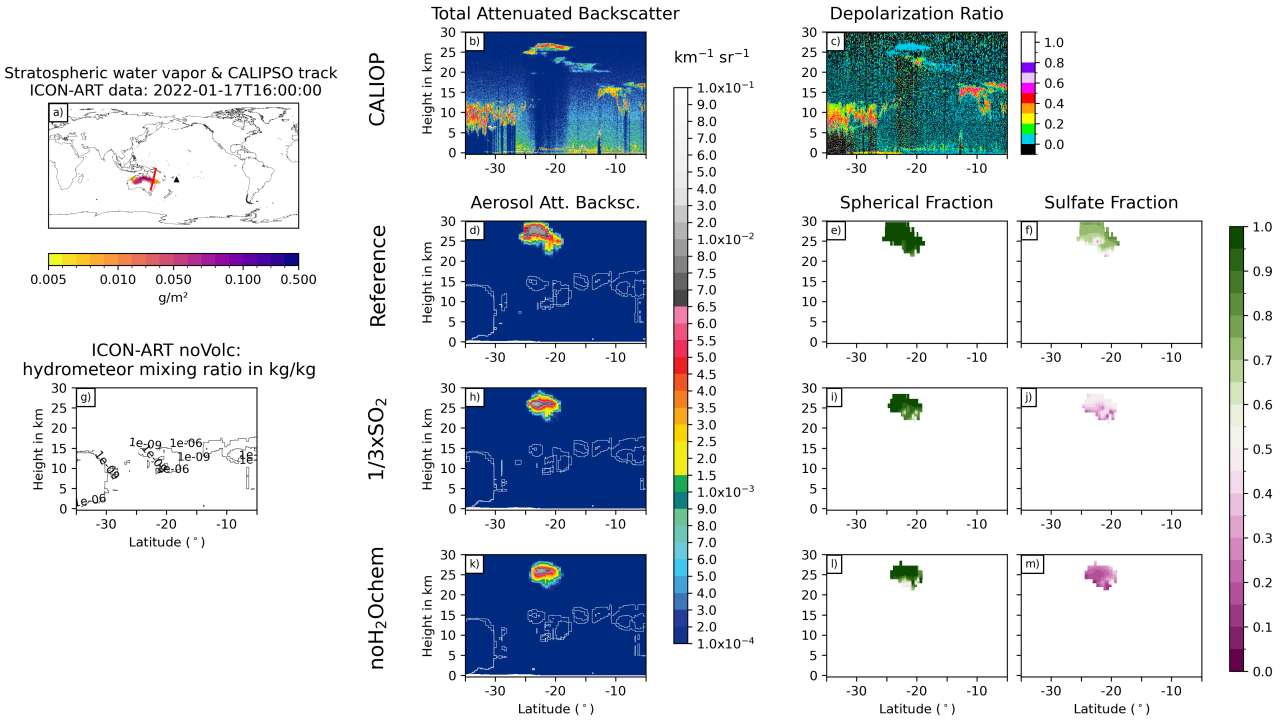

Figure D2. As Fig. 6, but for 17 January, 2022 at 16:00 UTC

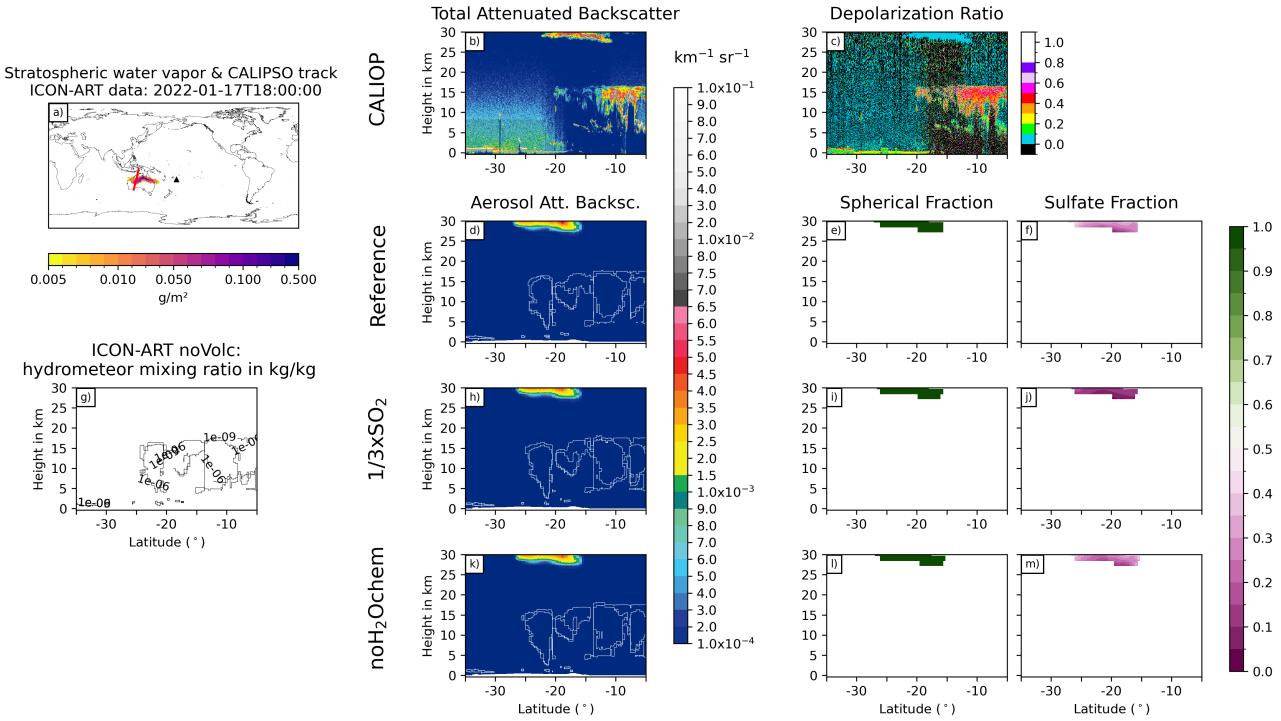

Figure D3. As Fig. 6, but for 17 January, 2022 at 18:00 UTC

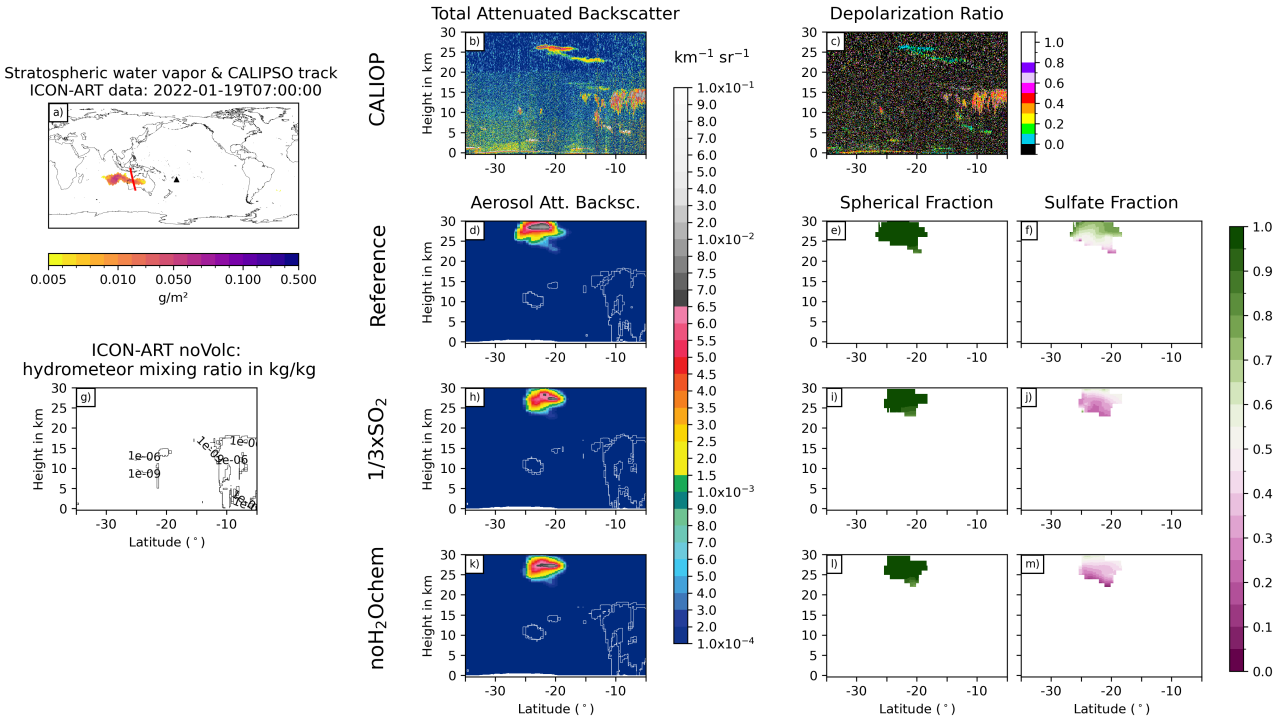

Figure D4. As Fig. 6, but for 19 January, 2022 at 7:00 UTC

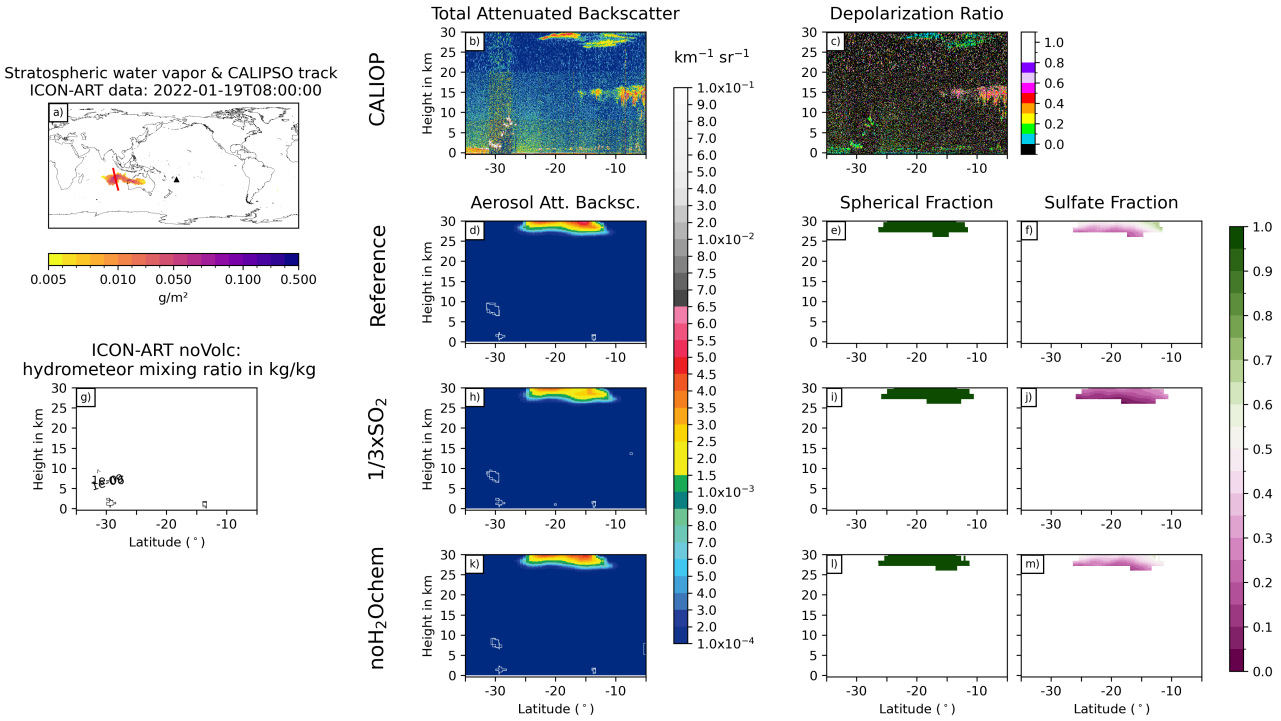

Figure D5. As Fig. 6, but for 19 January, 2022 at 8:00 UTC

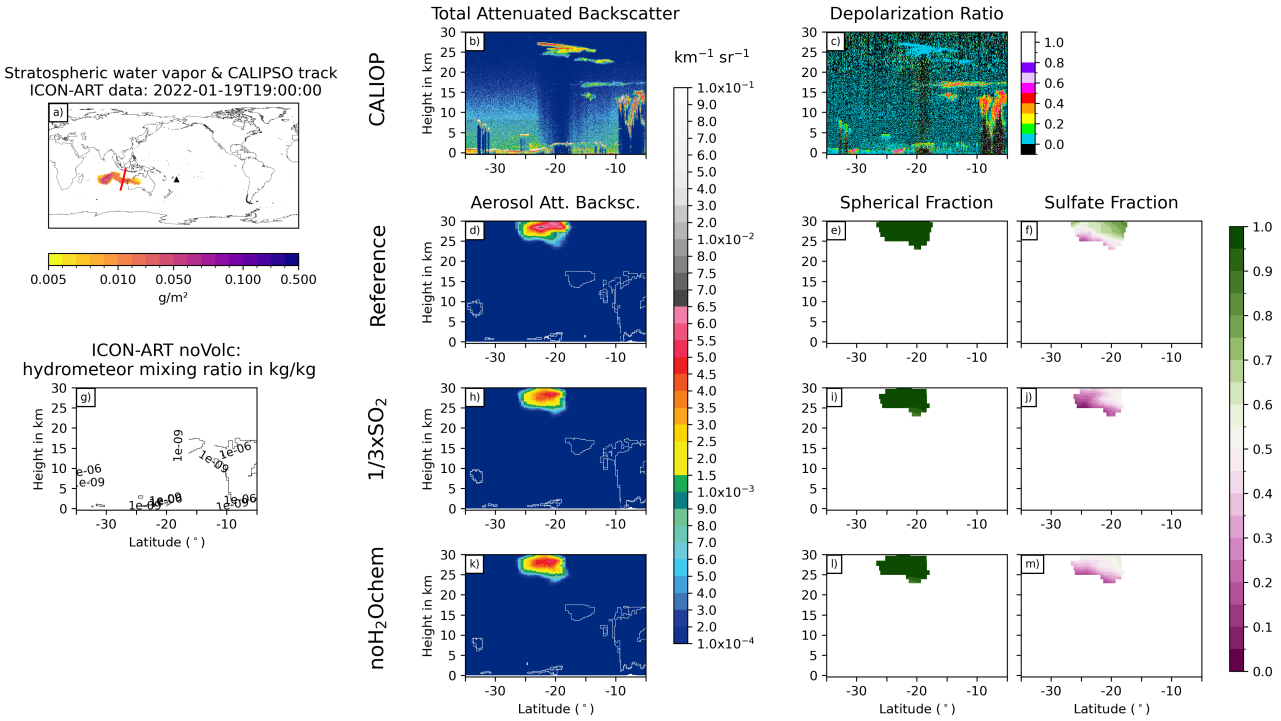

Figure D6. As Fig. 6, but for 19 January, 2022 at 19:00 UTC

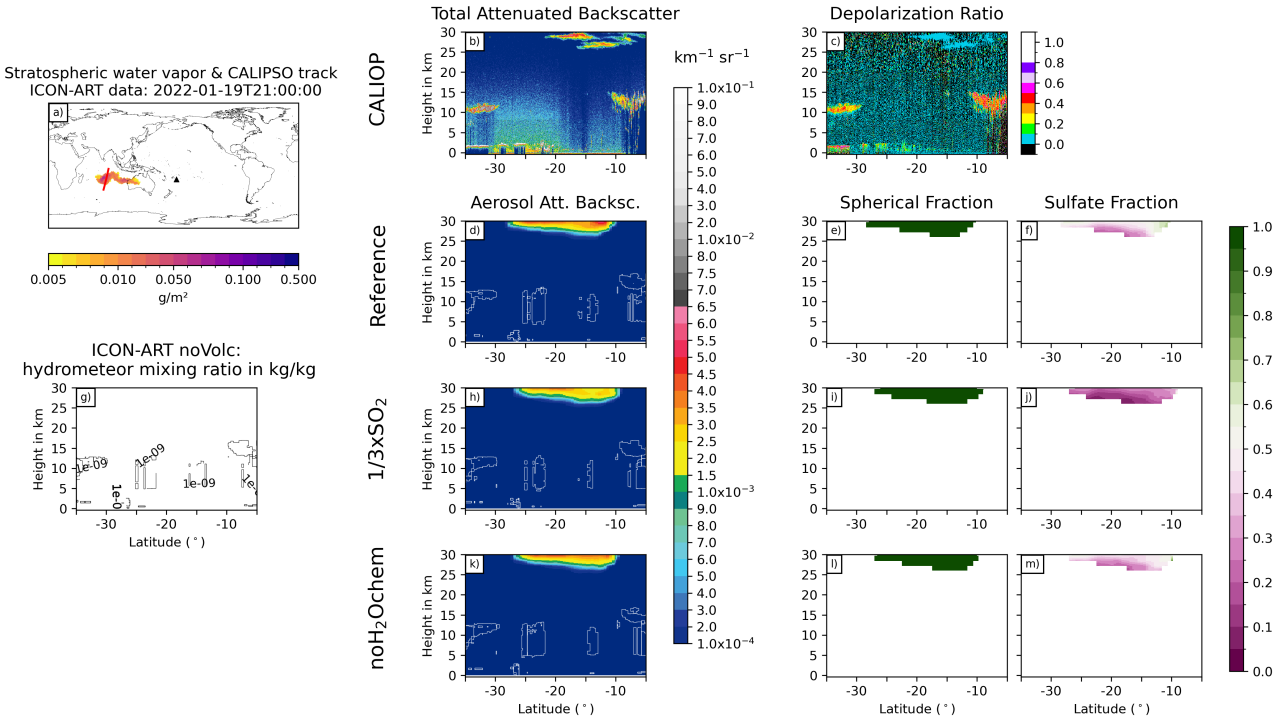

Figure D7. As Fig. 6, but for 19 January, 2022 at 21:00 UTC